Geoacoustic characterization of a range-dependent environment

by

MARK RYAN FALLAT
B.Sc., University of Victoria, 1997
M.Sc., University of Victoria, 1999

A Dissertation Submitted in Partial Fulfillment of the
Requirements for the Degree of

DOCTOR OF PHILOSOPHY

in the School of Earth and Ocean Sciences.

We accept this dissertation as conforming to the required standard.

Supervisors: Dr. Stan E. Dosso & Dr. Peter L. Nielsen

Abstract

Acoustic propagation in the underwater environment can be significantly influenced by interaction with the seafloor, particularly in shallow water areas. Therefore, a knowledge of the geoacoustic properties is essential to model acoustic propagation in shallow water environments. This thesis develops a technique for characterizing a range-dependent environment by combining the results from a series of short-range, range-independent geoacoustic inversions along a track. The experimental configuration involves a towed source and horizontal array. The analysis is carried out using two algorithms. The first is the hybrid inversion algorithm adaptive simplex simulated annealing (ASSA) which provides optimal estimates of the geoacoustic parameters, and the second is the fast Gibbs sampler (FGS) which provides a Bayesian uncertainty analysis. The uncertainty analysis provides a way of discerning whether variations in the inversion results are due to range-dependent features of the environment or simply due to uncertainty/variability in the results.

Acoustic data from the MAPEX 2000 and BOUNDARY 2003 experiments, conducted in the Strait of Sicily, Mediterranean Sea, are used in the analysis. These data sets were recorded over essentially the same range-dependent track but with different experimental configurations (i.e., different array lengths, sensor spacing and source frequencies). Ground-truth information in the form of core measurements and a high-resolution seismic profile were also collected and indicated a range-dependent environment with a low-speed sediment layer that pinched out along the track.

ASSA is initially applied to synthetic data based on the experiments to refine the inversion procedures (e.g., to determine an effective environmental parameterization). ASSA is then applied to invert MAPEX 2000 and BOUNDARY 2003 experimental

data with results that are generally in good agreement with the ground-truth information. A major issue with this analysis is deciding on an appropriate environmental parameterization based on the resolving power of the data. It is found that a simplified model of the environment based on two layers achieves the most reliable results. Also, the MAPEX 2000 data generally provided more accurate and consistent parameter estimates.

The FGS algorithm is also applied to the MAPEX 2000 data, with results that generally agree with the ground-truth information and the ASSA inversion results. This analysis shows that the large-scale variations in the ASSA results are actually due to environmental range-dependence and not another source of variability. However, the smaller-scale variations appear to be the result of uncertainty/variability in the ASSA inversion results. Overall, the work in this thesis verifies that towed HA data are capable of providing estimates of the dominant range-dependent features of an environment.

Examiners:

Contents

List of Figures

List of Tables

Acknowledgements

I would like to begin by thanking my friends and family who over the past 12 years have provided me with endless support and encouragement. I would also like to extend thanks to the various staff at the NATO Undersea Research Centre (formerly SACLANT) who have twice welcomed and supported me. Without them and without the Centre a great deal of this work would not be possible.

There are several people I need to thank for specific help. Gaetano Canepa for his help with LaTeX. This document would look terrible without you. Grazie Mille Caro! Mark Prior who over the past three years has had to look at my results plotted on a seismic profile so many times that I am sure he dreams about it now.

Jeg vil gene takke Peter Nielsen for hans støtte, den direkte væremädd og den altid opmuntrende holdning i løbet af projektet. Tak!

Stan, it is essentially impossible for me to articulate how much your support, guidance and time has meant to me during this work. For eight years now you have been guiding me on the trip of my life and I only wish that one day I can return the favour. Thank you!

Finally, this work is dedicated to Jamie.
For being there, then, now, always!
I love you!

Chapter 1

Introduction

1.1 Geoacoustic Inversion

To predict accurately acoustic propagation in an underwater environment requires a knowledge of the geoacoustic properties of the seafloor (e.g., sediment layer structure, compressional wave speeds, densities and attenuations). This is particularly true in a shallow water environment where the acoustic energy continuously interacts with the seafloor. In some environments the dependence of the acoustic propagation on the seabed is complicated by the range-dependent variation of the geoacoustic properties. Knowledge of these properties is of particular concern for sonar applications which require acoustic propagation predictions over a range of many kilometers. Unfortunately, existing geoacoustic databases have neither the required accuracy nor the spatial resolution for most shallow water sonar applications (Ferla & Jensen, 2003). In recent years, it has been shown that inversion techniques can provide a viable method of estimating geoacoustic properties from recorded acoustic data.

To date, most geoacoustic inversion work has utilized data recorded at a vertical array (VA) of sensors (Collins, Kuperman, & Schmidt, 1992; Dosso, Yeremy,

Ozard, & Chapman, 1993; Lindsay & Chapman, 1993; Gerstoft, 1994, 1995; Fallat & Dosso, 1998; Fallat, Nielsen, & Dosso, 2000). The drawbacks to this is that VA's are difficult and expensive to deploy. Therefore, the standard practice is to survey regions (over several kilometers range) using a single VA deployment. Unfortunately, spatial variability in the water column over these ranges can significantly degrade geoacoustic inversions results (Siderius, Nielsen, Sellschopp, Snellen, & Simons, 2001). Further, to invert for range-dependent geoacoustic properties using a single VA deployment requires that both the environmental parameterization and the propagation model be range dependent, substantially increasing the number of unknown parameters and the difficulty of the inversion. Range-dependent inversion of VA data is a challenging problem. Gerstoft and Gingras (1996) inverted VA data from a mildly range-dependent environment in the Mediterranean Sea. They were able to estimate accurately the sound speed structure of the water column but were unable to estimate reliably the bottom properties. Pignot and Chapman (2001) matched travel times and magnitudes of ray arrivals at a VA to estimate geoacoustic properties of a range-dependent environment. They used a two-stage inversion procedure which first determined the experimental parameters (e.g., range and source/receiver depths) and then held those parameters fixed and estimated the geoacoustic properties in the second stage. The inversion procedure consisted of representing the range-dependent environment as a series of range-independent segments and estimating the geoacoustic properties of each segment sequentially, moving out in range (holding previous segment values fixed). They also estimated multiple bottom layers sequentially downward. More recently, in 2001, a workshop was dedicated to the inversion of simulated, noise-free, range-dependent data that showcased many of the state-of-the-art techniques for range-dependent inversion (Chapman, Chin-Bing, King, & Evans, 2003).

An alternative to using a VA for geoacoustic inversion is to employ a towed

horizontal array (HA). Several studies to date have utilized HA data for geoacoustic inversion. Jesus and Caiti (1996) and Caiti et al. (1996) carried out inversions on single frequency HA data with moderate success and provided an overview of potential improvements for the inversion technique. Siderius et al. (2002) analyzed HA data to examine the feasibility of inversion with an emphasis on comparing the results from HA data with results from VA data . They inverted a small number of data sets from along a track in an attempt to estimate gross range-dependent structure of the environment, but with no comparison to "ground truth" (i.e., independent measurements of the geoacoustic properties such as core measurements and high-resolution seismic data). Battle et al. (2003) used tow-ship noise recorded at a towed HA for inversion of the sound speed in a half space at several points along a track.

To date, most geoacoustic inversion studies have focused on determining an optimal set of properties to describe the environment. One method of accomplishing this is matched field inversion (MFI). MFI is a forward-modelling approach to inversion where the goal is to determine a set of model parameters that minimizes some measure of mismatch between observed and modelled acoustic field data. This is a difficult nonlinear problem which often involves a large parameter space (10 or more parameters) that contains many local minima. MFI requires a reasonably descriptive model parameterization which must include both environmental parameters (e.g., number of layers, layer properties) and any experimental properties that are not know to sufficient accuracy (e.g., source and receiver depths, ranges). The environmental parameterization must also include physically meaningful search bounds which are often based on *a priori* information and/or empirical data. An acoustic propagation model which achieves a suitable trade-off between accuracy and speed is also required. An appropriate mismatch function that exploits the available information content of the data must also be employed. Finally, an effective optimization algorithm must be applied to determine the set of parameters that minimizes the mismatch.

A variety of optimization algorithms have been applied to MFI. Global optimization algorithms are the most popular methods and are designed to widely search the parameter space by using a random process to repeatedly perturb the model parameters and include the ability to escape local minima in the mismatch function. These methods include algorithms such as simulated annealing (SA) and its variants (Collins et al., 1992; Dosso et al., 1993; Lindsay & Chapman, 1993; Fallat & Dosso, 1998) and genetic algorithms (GA) (Gerstoft, 1994; Heard, Hannay, & Carr, 1998; Siderius, Gerstoft, & Nielsen, 1998; Gerstoft & Michalopoulou, 1998).

Hybrid methods which combine a global optimization with a local (gradient-based) search procedure have also been applied to geoacoustic inversion. Gerstoft (1995) combined GA with a local search based on a Gauss-Newton approach and applied the method to synthetic and measured data. Fallat et al. (1999) developed the simplex simulated annealing algorithm which combines SA and the downhill simplex method (DHS) (Nelder & Mead, 1965; Press, Teukolsky, Vetterling, & Flannery, 1992). They compared their algorithm to both SA and DHS using simulated data. Another method developed by Musil et al. (1999) combined GA with DHS. Dosso et al. (2001) developed an adaptive hybrid algorithm based on SA and DHS and applied it to a series of benchmark testcases. Recently, Gerstoft (1998) has included a local search based on Powell's method (Press et al., 1992) into GA.

In addition to these global and hybrid algorithms other approaches to optimization have also been applied. Several studies have applied local (gradient-based) methods to the geoacoustic inversion problem (Rajan, Lynch, & Frisk, 1987; Zala & Ozard, 1998; Fallat & Dosso, 1999), and grid search methods (Tolstoy, 1998). More recently, methods such as the Tabu algorithm (Michalopoulou & Ghosh-Dastidar, 2004) and differential evolution (vanMoll & Simons, 2004; Snellen, Simons, & vanMoll, 2004) have also been utilized. Two major workshops, with accompanying special journal issues (Chapman, Tolstoy, & Brooke, 1998; Chapman et al., 2003), were dedicated to

investigating and comparing MFI algorithms using noise-free synthetic data.

Recently, work has been done on not only determining the optimal set of model parameters but also attempting to quantify the uncertainty associated with these parameter estimates. This uncertainty analysis is based on a Bayesian formulation in which the solution to an inverse problem is characterized by the posteriori probability distribution (PPD) (Tarantola, 1987; Sen & Stoffa, 1995). Gerstoft (1994) employed a Bayesian formulation to an empirical objective function sampled using the final generations of GA inversions. This technique was updated by Gerstoft and Mecklenbräuker (1998) who developed a likelihood-based approach for estimating the PPD. The method was again based on using the final generations of GA inversions which resulted in an unknown bias being introduced into the uncertainty estimates (Gerstoft & Mecklenbräuker, 1998). An alternative approach was developed by Dosso (Dosso, 2002; Dosso & Nielsen, 2002) which used a Gibbs sampling (GS) method that provides an unbiased sampling of the PPD. Standard GS can be computationally slow, therefore Dosso applied several modifications that have been used to increase the efficiency of SA optimizations. The resulting fast Gibbs sampling (FGS) algorithm was shown to provide rigorous estimates of the PPD with substantially less computation time than other methods (Dosso, 2002).

This thesis develops a technique for characterizing a range-dependent environment by combining the results of a series of short-range, range-independent inversions. This is part of a "through-the-sensor" strategy that intends to make use of existing sonar systems to determine environmental properties. The approach is illustrated schematically in Fig. 1.1. The method consists of towing a source and array along a track and carrying out an inversion for each source ping. The individual inversion results are then combined in an attempt to describe the range-dependent environment along a track. The analysis here consists of two components. The first component uses a hybrid inversion algorithm to determine optimal estimates of the properties at

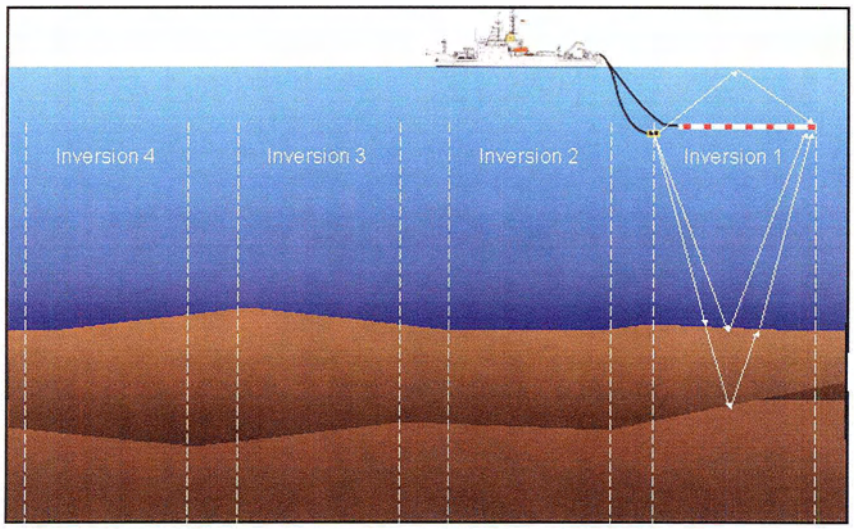

Figure 1.1: Schematic diagram of the experimental setup.

various points along the track. These estimates are then compared to "ground-truth" information to validate the results. The second component is a Bayesian analysis of the uncertainties associated with the environmental properties. This analysis is vital to discern whether variations in the inversion results are due to range-dependent features of the environment or simply uncertainty/variability.

1.2 Outline of Work

This section presents a brief overview of the remainder of the thesis. In Chapter 2, an overview of the theory applied in this work is provided. This includes a basic review of inverse theory, an explanation of the Bayesian formulation to the inverse problem, a review of matched field inversion, and a description of the algorithms and

propagation models that are used in this work.

A description of the experiments is given in Chapter 3. The MAPEX 2000 and BOUNDARY 2003 experiments provided an excellent opportunity to investigate the inversion technique on different data sets recorded in the same area. The major differences between these data sets were the array length, the sensor spacing and the source frequencies. This chapter provides information about the experimental procedures and considers the acoustic data. Also included are descriptions of the environmental data (core and seismic) collected at the experimental site which serve as ground truth.

In Chapter 4, three different optimization algorithms are investigated to determine which algorithm induces the least amount of variability in the inversion results. It is important to consider the variability inherent in the inversion procedure itself, i.e., the repeatability or consistency of results simply due to the different random initializations of the algorithm. This is particularly important here because this work combines results from independent inversions to produce a larger representation of the environment. This task requires confidence that the variation in the properties is actually due to range-dependence of the environment and not a result of algorithm-induced variability.

The algorithms are examined using noise-free and noisy synthetic data from the 1997 Geoacoustic Inversion Workshop (Chapman et al., 1998) and measured data from the MAPEX 2000 experiment. The algorithms considered are GA (Gerstoft, 1994; Sen & Stoffa, 1995), fast simulated annealing (FSA) (Szu & Hartley, 1987; Liu, Hartzell, & Stephenson, 1995; Fallat & Dosso, 1998), and a hybrid inversion algorithm, adaptive simplex simulated annealing (ASSA) (Fallat & Dosso, 1999; Dosso et al., 2001). The FSA and ASSA algorithms were implemented by the author while the inversion package SAGA (Gerstoft, 1998) was employed for GA. SAGA has been applied extensively to such problems and is generally accepted as a standard geoa-

coustic inversion tool. It was found that ASSA induced the least amount of variability and is therefore employed for the remainder of the analysis.

In Chapter 5, the ASSA inversion analysis of the MAPEX 2000 and BOUNDARY 2003 data is described. The chapter first considers the inversion of synthetic data to examine issues of sediment layer resolution and parameter sensitivity in a controlled manner, then proceeds to describe the inversion results for the experimental data. The results of the individual inversions are combined to produce a representation of the range-dependent environment and compared to ground-truth data.

In Chapter 6, the results of the FGS uncertainty analysis are provided. This analysis includes a comparison of the FGS results to the results from the ASSA inversions and to the ground-truth data. Quantifying the uncertainty in the geoacoustic properties is important to discern if variation in the inversion results is due to the actual range-dependence of the environment. Finally, Chapter 7 summarizes the work in this thesis and provides a discussion of the conclusions.

Chapter 2

Inverse Theory

2.1 The Inverse Problem

Inverse theory can be defined as the estimation of a set of parameters of a postulated model for a physical system from a set of observations of a process which interacts with the system. For the problem considered in this thesis, the physical system is the ocean environment and the process is acoustic propagation through this environment. The forward problem ($\mathbf{F}$) can be defined as given a set of model parameters $\mathbf{m}$ (geoacoustic properties, uncertain experimental parameters, etc) compute the acoustic data $\mathbf{d}$ that would be observed,

$$\mathbf{F}[\mathbf{m}] = \mathbf{d}. \tag{2.1}$$

The inverse problem can be defined as given a set of acoustic data, determine the model parameters that produced the data, i.e.,

$$\mathbf{m} = \mathbf{F^{-1}}[\mathbf{d}], \tag{2.2}$$

where the inverse operator $\mathbf{F}^{-1}$ is used for notational purposes only since it may not exist. The forward problem defines some physical process and therefore will generally

have a solution that exists, is unique and stable. Stability generally indicates how errors in the model parameters propagate into the acoustic modelling (Sen & Stoffa, 1995). In particular, a stable solution will be one where small changes in model parameters result in small changes in the acoustic data. Unfortunately, the same is not true for the inverse problem which is generally non-unique and in many cases unstable.

Inverse problems can be separated into two categories: linear and nonlinear, although in some cases weakly nonlinear problems can be linearized. The problem considered in this work is strongly nonlinear and therefore a fully nonlinear solution is developed.

2.2 Bayesian Formulation

Generally, nonlinear inverse problems require the application of numerical methods to obtain a solution. This section summarizes a Bayesian formulation for nonlinear inverse problems (Tarantola, 1987; Sen & Stoffa, 1995; Gerstoft & Mecklenbräuker, 1998; Dosso, 2002; Dosso & Nielsen, 2002). Let $\mathbf{m}$ and $\mathbf{d}$ define model and data vectors of elements m_i and d_i, respectively. If both m_i and d_i are considered to be random variables then Bayes' rule can be used to define the following conditional probability:

$$P(\mathbf{m}|\mathbf{d}) = \frac{P(\mathbf{d}|\mathbf{m})P(\mathbf{m})}{P(\mathbf{d})}. \tag{2.3}$$

In Eqn. 2.3, $P(\mathbf{m}|\mathbf{d})$ defines the conditional probability density function (PDF) of the model $\mathbf{m}$ given a data vector $\mathbf{d}$. $P(\mathbf{d}|\mathbf{m})$ is the PDF of $\mathbf{d}$ given $\mathbf{m}$ and $P(\mathbf{m})$ is the PDF of $\mathbf{m}$ independent of $\mathbf{d}$. Finally, $P(\mathbf{d})$ is the PDF of $\mathbf{d}$. Equation 2.3 can be simplified by noting that the denominator $P(\mathbf{d})$ is independent of the model vector

and can be considered constant, leading to

$$P(\mathbf{m}|\mathbf{d}) \propto P(\mathbf{d}|\mathbf{m})P(\mathbf{m}). \tag{2.4}$$

Substituting a (fixed) observed data set $\mathbf{d}^{obs}$ into $P(\mathbf{d}|\mathbf{m})$ leads to the likelihood function, $L(\mathbf{d}^{obs}|\mathbf{m})$, which is interpreted as a function of $\mathbf{m}$. Equation 2.4 then becomes

$$P(\mathbf{m}|\mathbf{d}^{obs}) \propto L(\mathbf{d}^{obs}|\mathbf{m})P(\mathbf{m}). \tag{2.5}$$

Here, $P(\mathbf{m})$ is the prior PDF which represents the available *a priori* information about the model independent of observed data. $P(\mathbf{m}|\mathbf{d}^{obs})$ is the probability of the model $\mathbf{m}$ given the observed data and prior and is called the posterior probability distribution (PPD).

Formulating the likelihood function $L(\mathbf{d}^{obs}|\mathbf{m})$ requires information about the statistical distribution of the data errors. This must include both theory errors (due to the idealized environment, approximate propagation modelling, etc) and measurement errors (uncertainty in sensor positions, source characteristics, etc). Generally the likelihood function can be expressed as

$$L(\mathbf{d}^{obs}|\mathbf{m}) \propto \exp[-E(\mathbf{m}, \mathbf{d}^{obs})], \tag{2.6}$$

where $E(\mathbf{m}, \mathbf{d}^{obs})$ is the appropriate error function (described in Sec. 2.5). Substituting this into Eqn. 2.5 and normalizing results in

$$P(\mathbf{m}|\mathbf{d}^{obs}) = \frac{\exp[-\phi(\mathbf{m}, \mathbf{d}^{obs})]}{\int_{\mathcal{M}} \exp[-\phi(\mathbf{m}', \mathbf{d}^{obs})] d\mathbf{m}'}, \tag{2.7}$$

where $\phi(\mathbf{m}, \mathbf{d}^{obs}) = E(\mathbf{m}, \mathbf{d}^{obs}) - \ln[P(\mathbf{m})]$ is a generalized misfit that includes both data and prior terms, and the integral in the denominator spans the multi-dimensional model space $\mathcal{M}$.

From a Bayesian viewpoint, the general solution to the inverse problem can be characterized by the PPD given in Eqn. 2.7. However, to interpret the PPD,

$P(\mathbf{m}|\mathbf{d}^{obs})$, requires the computation of properties of the distribution such as the maximum *a posteriori* (MAP) model estimate, mean model estimate, covariance matrix and marginal probability distributions, which are given by the following

$$\hat{\mathbf{m}}_{\text{MAP}} = \text{arg}_{\text{max}}\{P(\mathbf{m}|\mathbf{d}^{obs})\}, \tag{2.8}$$

$$\hat{\mathbf{m}} = \int_{\mathcal{M}} \mathbf{m}' P(\mathbf{m}'|\mathbf{d}^{obs}) d\mathbf{m}', \tag{2.9}$$

$$\mathbf{C} = \int_{\mathcal{M}} (\mathbf{m}' - \hat{\mathbf{m}})(\mathbf{m}' - \hat{\mathbf{m}})^T P(\mathbf{m}'|\mathbf{d}^{obs}) d\mathbf{m}', \tag{2.10}$$

$$P(m_i|\mathbf{d}^{obs}) = \int_{\mathcal{M}} \delta(m_i' - m_i) P(\mathbf{m}'|\mathbf{d}^{obs}) d\mathbf{m}', \tag{2.11}$$

where δ represents the Dirac delta function and multi-dimensional marginal probability distributions are defined with expressions similar to Eqn. 2.11. Another useful quantity is the correlation matrix ($\mathbf{C_R}$) which quantifies the correlations between all parameters. The correlation matrix is computed by normalizing the elements of the covariance matrix (Eqn. 2.10) to remove the influence of the different parameter scales and units. The ij^{th} element of $\mathbf{C_R}$ is defined by

$$\mathbf{C}_{\mathbf{R}ij} = \frac{\mathbf{C}_{ij}}{\sqrt{\mathbf{C}_{ii}\mathbf{C}_{jj}}}. \tag{2.12}$$

The elements of this matrix have values between ± 1 with $+1$ (-1) representing a perfect positive (negative) correlation between two parameters and near-zero values representing uncorrelated parameters. Computing these properties for a nonlinear problem, such as geoacoustic inversion, requires a numerical approach. In particular, the MAP estimate can be obtained by optimizing the PPD, or minimizing the misfit $\phi(\mathbf{m}, \mathbf{d}^{obs})$, while the other properties require evaluating multi-dimensional integrals. These two procedures are described in more detail in the following sections.

2.3 Optimization of the PPD

As stated in Sec. 2.2, one of the PPD properties of interest is the MAP model estimate. For more than a decade the geoacoustic inversion community has focused considerable effort on finding optimal parameter estimates (equivalent to the MAP estimate). This effort has been primarily centered around developing strategies and algorithms to effectively and efficiently minimize a nonlinear mismatch function. Currently, there are many different algorithms available for this purpose; in this study three are investigated: fast simulated annealing (Szu & Hartley, 1987; Liu et al., 1995), adaptive simplex simulated annealing (Fallat & Dosso, 1999; Dosso et al., 2001) and genetic algorithms (Gerstoft, 1994, 1995; Sen & Stoffa, 1995).

2.3.1 Fast Simulated Annealing

Simulated annealing (SA) (Kirkpatrick, Gelatt, & Vecchi, 1983; Sen & Stoffa, 1995) is a well known optimization algorithm that is based on the physical process of annealing. In annealing, a substance is heated until it is in a high-energy state and then allowed to cool slowly so that a stable low-energy state is achieved (Sen & Stoffa, 1995). If cooled slowly enough the low-energy state should be the lowest possible energy state (i.e., the global minimum).

In SA the state of a model $\mathbf{m}$ with an objective function $\phi(\mathbf{m})$ (often referred to as energy in analogy with annealing) is given by the Gibbs distribution

$$P_G(\mathbf{m}) = \frac{\exp[-\phi(\mathbf{m})]/T}{\sum \exp[-\phi(\mathbf{m})]/T}, \tag{2.13}$$

where T is the absolute temperature and the sum in the denominator spans all possible models. SA consists of a series of iterations involving random perturbations to the set of model parameters. Perturbations that decrease the energy are always accepted while perturbations that increase the energy are accepted if a uniform random number

ξ on $[0,1]$ satisfies

$$\xi \leq \exp\left[\frac{-\Delta\phi}{T}\right]. \tag{2.14}$$

This procedure is known as the Metropolis algorithm (Metropolis, Rosenbluth, M. Rosnebluth, & Teller, 1953). Markov-chain analysis verifies that with sufficient sampling the Metropolis algorithm provides models distributed according to the Gibbs distribution (Sen & Stoffa, 1995).

SA optimization is based on Metropolis Gibbs sampling while slowly reducing the temperature, thereby reducing the probability of accepting models that increase the energy. The algorithm has the ability to escape local minima in search of a better solution, but eventually, as T decreases, the algorithm spends more time searching regions with lower energy values. Eventually the algorithm will converge to a solution that should approximate the global minimum.

Several algorithm parameters must be set correctly for an effective optimization including:

1) the starting temperature,

2) the rate of reducing T and

3) the number and type of perturbations.

These properties define what is commonly called the annealing schedule. Adopting an annealing schedule that is too fast (i.e., decreases T too quickly or allows too few perturbations) can lead to a sub-optimal solution. Alternatively, implementing an annealing schedule that is too slow will waste computation time. Unfortunately, there is no predetermined way to define an appropriate annealing schedule. The schedule is generally problem specific and therefore requires some experimentation and familiarity with the problem. A "rule-of-thumb" for determining an appropriate

value of the starting temperature is to require at least 90% of all perturbations (uphill and downhill) are accepted initially.

In many cases SA has proven to be an effective optimization algorithm, but it is not without limitations. SA can be relatively inefficient near convergence, where instead of concentrating on moving locally downhill it typically attempts many random perturbations that increase E and are not accepted. Also, as SA is based on perturbations along the parameter axes, the algorithm can be inefficient for correlated parameters that give rise to narrow valleys in the parameter space that are not aligned with the parameter axes.

These limitations have lead to the development of different variations of SA. In this work, a variant of fast simulated annealing (FSA) (Szu & Hartley, 1987; Liu et al., 1995) is used. The FSA algorithm has a simple yet effective modification that makes it a more efficient optimization algorithm than standard SA (although not all of the shortcomings of standard SA are overcome). The modification is using a temperature-dependent Cauchy distribution to produce the parameter perturbations instead of a uniform distribution. A Cauchy distribution has the desirable properties of a Gaussian-like peak and Lorentzian tails which provide concentrated local sampling of the parameter space while allowing the occasional large perturbation. The Cauchy distribution is implemented in the following way. First assume that the parameters have lower and upper bounds denoted by m_i^- and m_i^+ respectively. Each model parameter is perturbed according to

$$m_i = m_i' + \varphi_m \psi, \tag{2.15}$$

where m_i' is the value of the model parameter prior to the perturbation and φ_m is the perturbation factor which is randomly selected from the interval $[-\Delta m_i, \Delta m_i]$. The quantity Δm_i is the size of the search interval for the particular model parameter and is given by $\Delta m_i = m_i^+ - m_i^-$. The quantity ψ is a temperature-dependent Cauchy-

distributed random variable given by

$$\psi = [T_j/T_0] \tan[\eta(\pi/2)]. \tag{2.16}$$

In Eqn. 2.16, η is a uniform random variable on $[-1, 1]$, T_j is the temperature at the j^{th} step and T_0 is the starting temperature.

The above procedure yields perturbations that are uniformly distributed in direction and Cauchy distributed in distance. At high T, large perturbations dominate the search, while at low T the exploration is dominated by smaller perturbations and thus a more localized search is carried out. However, because of the shape of the Cauchy distribution large perturbations are possible at all temperatures.

2.3.2 Adaptive Simplex Simulated Annealing

Adaptive simplex simulated annealing (ASSA) (Fallat & Dosso, 1999; Dosso et al., 2001) is a hybrid optimization algorithm which combines the downhill simplex (DHS) method with FSA. The resulting algorithm has been found to be more efficient and more effective then either of the individual algorithms for geoacoustic inversion (Dosso et al., 2001).

The DHS algorithm is based on an intuitive geometric scheme for moving downhill in the parameter space (Nelder & Mead, 1965; Press et al., 1992). Although DHS itself is not the most efficient algorithm for local optimization, it has the desirable qualities of not requiring the computation of partial derivatives or the solution of systems of equations. This means that each iteration is quite simple and efficient to compute.

The algorithm operates on a simplex of $M + 1$ models in a M-dimensional space. Figure 2.1(a) shows a schematic diagram of a simplex for $M = 3$. The initial simplex is chosen at random from the parameter space and in order to move downhill, the simplex undergoes a series of transformations. Each model in the simplex is first

ranked according its misfit, ϕ. The algorithm initially attempts to improve the model with the highest value of ϕ by reflecting it through the face of the simplex containing the model with the lowest ϕ value [Fig. 2.1 (b)]. If the new model now has the lowest ϕ in the simplex, then an extension by a factor of two in the same direction is attempted [Fig. 2.1 (c)]. If the reflection results in a model that still has the highest ϕ, the reflection is rejected and a contraction by a factor of two towards the model with the lowest ϕ is attempted [Fig. 2.1 (d)]. If none of these steps have decreased the misfit then a multiple contraction by a factor of two in all dimensions toward the model with the lowest ϕ is performed [Fig. 2.1 (e)]. This process is repeated until the difference between the models with the highest and lowest values of ϕ, relative to their average, is less than some tolerance ε,

$$\frac{\phi_{hi} - \phi_{lo}}{(\phi_{hi} + \phi_{lo})/2} < \varepsilon, \tag{2.17}$$

or until a maximum number of iterations have been completed.

ASSA combines FSA and the DHS method into an adaptive optimization scheme. Unlike standard FSA, the ASSA algorithm operates on a simplex of models rather than a single model. Also, instead of employing a purely random model perturbation, a DHS step followed by a random perturbation is used to compute the new model parameters. This new model is then evaluated for acceptance using the criterion for standard SA (Eqn. 2.14).

In ASSA, the relative size of the DHS and random steps is controlled adaptively based on the average size of the recently accepted perturbations. This is based on the assumption that the running average of the size of the most recently accepted perturbations will provide a reasonable indication of an effective size for new perturbations. This also assumes that the size of the new perturbations is not limited by the original distribution of the search interval and that perturbations are large enough to characterize the relevant regions of the search space.

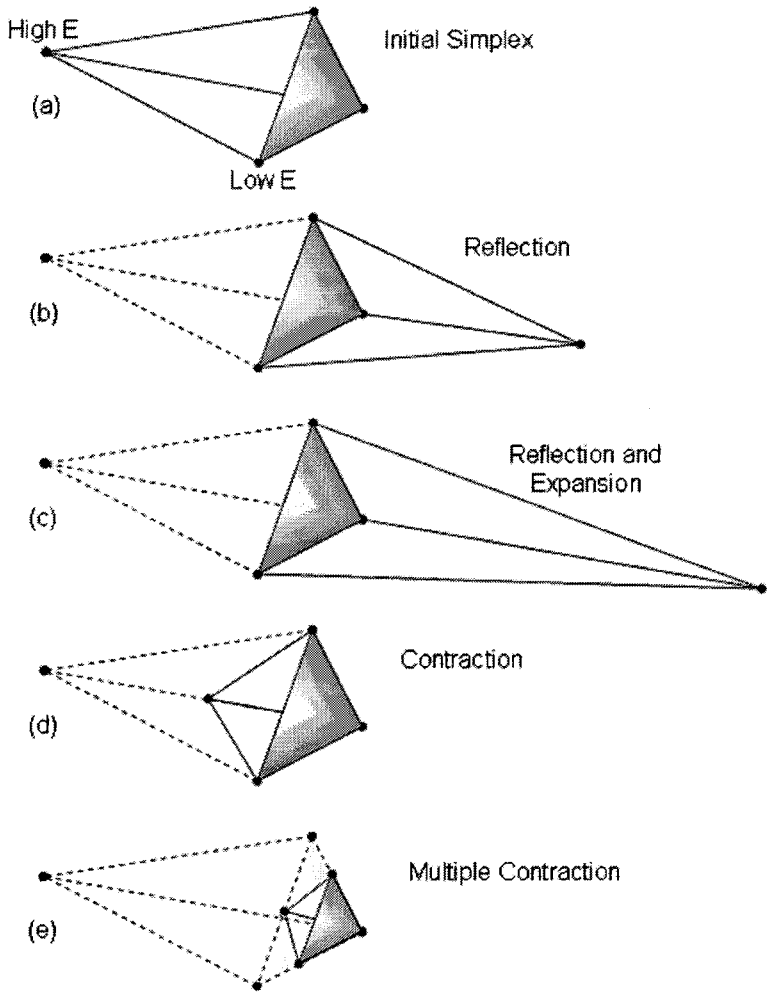

Figure 2.1: Downhill simplex steps in three dimensions.

This procedure (i.e., a DHS step followed by a random perturbation) perturbs all of the model parameters at once in such a way to combine both gradient-based and random components. The size of the random component is adaptively controlled for individual parameters. This individual control is particularly important for problems that involve parameters with a wide range of sensitivities. Also, by incorporating DHS steps the method overcomes the difficulties associated with parameter correlations and since the best model is always retained in the simplex the algorithm has a memory of the best model to date.

Several control parameters must be set by the user before an ASSA optimization can be carried out. These include the starting temperature, the temperature reduction factor, the number of iterations and the number of previously accepted models to include in the adaptive scaling. Generally, the starting temperature and the number of models included in the adaptive scaling do not significantly influence the inversions as long as reasonable values are used. The temperature reduction factor and the number of iterations can significantly influence the inversions and therefore must be set with a degree of care. Appropriate values for these parameters are not always known and are generally problem specific. A good guideline is to select a temperature reduction factor and the number of iterations such that the final temperature achieves a level that is several orders of magnitude lower than the expected mismatch.

2.3.3 Genetic Algorithms

In this thesis, the genetic algorithms (GA) package SAGA (Gerstoft, 1994, 1995, 1998) was used for some of the inversions. What follows is a description of the techniques applied in SAGA. GA are based on the biological process of evolution (Sen & Stoffa, 1995). GA are straightforward to understand but in practice the implementation can be complicated. The method starts with an initial population of models which

undergo a series of steps to try to reduce the misfit of the models. After these steps have been repeated a number of times the model with the lowest misfit is taken as the best estimate of the global minimum.

In GA, there are five basic steps: coding, selection, crossover, mutation, and replacement. The first step, coding, consists of describing the model using a binary coding system that results in a bit-string often referred to as a chromosome. The coding must represent all possible solutions for the various model parameters, which means that the search space for each parameter can be independently defined and its resolution or discretization can be specified individually. The coding system must also define the limits of the search space and the discretization of the search interval for each parameter.

The next step in GA is model selection. In selection, pairs of models from the population are chosen to form the parents of the next generation. The selection is based on the misfit of models and is a random process with the probability of a model being chosen decreasing with its misfit (i.e., the lower the misfit the more probable the model selection). In SAGA, the probability that the i^{th} model, of a population of Q models, will be selected is given by

$$P(\mathbf{m}_i) = \frac{1 - \phi(\mathbf{m}_i)}{\sum_{j=1}^{Q}[1 - \phi(\mathbf{m}_j)]}. \tag{2.18}$$

Once the models have been selected the new population is created using a process called crossover. In crossover, a single bit within each model parameter is randomly selected as the crossover point. Then, one of two possible operations can occur. First, all of the information, or bits, to the right of the selected point can be exchanged (this occurs with a pre-determined probability P_x). The other possibility is that there is no exchange of information which occurs with a probability of $1 - P_x$.

The next step in GA is mutation, which can often be done during the crossover step. Mutation is a random alteration of a single bit in the coded model. The rate

of mutation is pre-set by the user and may require some familiarization with the problem. A low mutation rate limits the randomness of the algorithm. Whereas, a high mutation rate will introduce a larger degree of randomness at the cost of computation time.

The final step is to replace the models of the old population with the new models. The new models replace the highest misfit members of the old population. By running the process of selection, crossover, mutation and replacement over many generations the models in the population will continue to lower their misfit until they approximate a minimum.

GA often have many control parameters that can be set, but most of these do not significantly influence the inversion as long as reasonable values are employed. Three important parameters are the number of populations, the number of generations for each populations, and the discretization of the parameter space. Discretizing the parameter space generally requires some knowledge of how sensitive the inversion is to a particular parameter. This will require some experimentation or familiarity with the problem. Choosing appropriate values for the number of populations the number of generations is generally problem specific but a good practice is to have fewer populations for more generations as opposed to many populations for fewer generations.

2.4 Sampling the PPD and Fast Gibbs Sampling

As stated in Sec. 2.2, in order to solve the multi-dimensional integrals in Eqns. 2.9-2.11 a numerical method must be used. Note that Eqns. 2.9-2.11 are all of the general

form

$$I = \int_{\mathcal{M}} f(\mathbf{m}')P(\mathbf{m}'|\mathbf{d}^{obs})d\mathbf{m}'. \tag{2.19}$$

There are several ways to integrate numerically a multi-dimensional function like Eqn. 2.19 (Sen & Stoffa, 1995), in this work importance sampling is employed. Importance sampling is based on the idea of concentrating the sampling in regions of the space that are "important" (i.e., that contribute the most to the integral). This means that the samples must be randomly drawn from a non-uniform distribution. Let $g(\mathbf{m})$ represent a generalized, non-uniform sampling function from which the model $\mathbf{m}_i$, is drawn. The integral can then take the following form

$$I = \int_{\mathcal{M}} \left[\frac{f(\mathbf{m}')P(\mathbf{m}'|\mathbf{d}^{obs})}{g(\mathbf{m}')}\right] g(\mathbf{m}')d\mathbf{m}' \approx \frac{1}{Q}\sum_{i=1}^{Q} \frac{f(\mathbf{m}_i)P(\mathbf{m}_i|\mathbf{d}^{obs})}{g(\mathbf{m}_i)}, \tag{2.20}$$

where Q is the number of models drawn. The challenging aspect of this problem is selecting an appropriate sampling function. Gibbs sampling (GS) is an approach that provides an effective method for importance sampling. Note that the probability used for GS (Eqn. 2.13) is equivalent in form to the PPD given by Eqn. 2.7 with $T = 1$. This means that if a large number of samples are drawn the GS will sample directly from the PPD. Therefore using GS for importance sampling results in a sampling function that is $g(\mathbf{m}) = P(\mathbf{m}|\mathbf{d}^{obs})$ and Eqn. 2.20 becomes

$$I \approx \frac{1}{Q}\sum_{i=1}^{Q} f(\mathbf{m}_i). \tag{2.21}$$

Fast Gibbs sampling (FGS) (Dosso, 2002; Dosso & Nielsen, 2002) is an efficient algorithm that has been developed for GS. GS generally requires a large number of samples; FGS uses several straightforward modifications to help decrease the total computation time by reducing the number of samples that are needed. The first modification involves rotating the parameter space (Collins & Fishman, 1995). This is done because correlations between parameters result in oblique valleys that do not

align with the parameter axes. In this case, perturbations along the parameter axes are inefficient. A similar problem occurs during optimization using SA which Collins and Fishman (1995) addressed by rotating the parameter space using an orthogonal transformation based on the covariance matrix of the gradient of the misfit. The FGS algorithm applies a similar approach with a slight change. Instead of computing the rotation matrix using the gradient of the misfit the rotation matrix is computed directly from the misfit.

In order to facilitate this modification an initial small number of samples (compared to the total number of samples) is collected to compute the covariance matrix $\mathbf{C}$. The rotation matrix is determined using eigenvalue decomposition

$$\mathbf{C} = \mathbf{A}\mathbf{\Lambda}\mathbf{A}^T, \tag{2.22}$$

where $\mathbf{\Lambda}$ is a diagonal matrix with elements λ_i consisting of the eigenvalues of $\mathbf{C}$ and $\mathbf{A}$ is an orthogonal matrix with columns $\mathbf{a}_i$ consisting of the corresponding eigenvectors. Rotated parameters are calculated by applying an orthogonal transformation

$$\hat{\mathbf{m}} = \mathbf{A}^T\mathbf{m}. \tag{2.23}$$

The perturbations are applied in the rotated parameter space and then rotated back to the original, physical parameter space by the following transformation

$$\mathbf{m} = \mathbf{A}\hat{\mathbf{m}}. \tag{2.24}$$

Once the parameters are back in the original space the modelled data can be computed and the misfit calculated.

The second modification involves an adaptive scheme to determine an effective perturbation size. FGS is usually initiated from a good model, e.g., the MAP estimate from a previous optimization. Initially, small perturbations are attempted but a growth factor is included so that perturbations significantly larger than the largest

accepted perturbation to that point are attempted. The size of the growth factor can be reduced at later stages in the sampling for efficiency.

Finally, the algorithm must have a convergence criterion to know when enough samples have been collected. The FGS algorithm employs a straightforward but effective method to test for convergence. Two parallel but independent samples are computed simultaneously and inter-compared periodically. When the maximum difference between the cumulative marginal distributions is small enough, the two samples are considered to have converged and they are then combined to create a single large sample from which the moments of the PPD are computed.

2.5 Matched Field Inversion

Matched Field Inversion (MFI) is a nonlinear inversion method based on forward modelling. The goal is to match the relative amplitude and phase of observed frequency-domain acoustic data with modelled acoustic data. The data consist of complex acoustic fields recorded at an array of sensors over a particular frequency band. The purpose is to determine a set of model parameters that minimizes the mismatch between measured and modelled fields. It is important that the model parameters are chosen to provide a reasonable approximation of the environment. Also, the mismatch function should be selected to make use of the available information content of the data.

Standard MFI typically assumes that the response from sensor to sensor can be modelled accurately. However, for the data analyzed here this proved not to be the case (Siderius et al., 2002). Possible reasons for this are poor calibration of the individual sensors and/or errors in the assumed sensor positions. Therefore, the processing applied here is incoherent in space (i.e., from sensor to sensor) and coherent in frequency at individual sensors, making use of prior measurements of the source

spectrum, as described in Chapter 3.

In a Bayesian formulation of MFI, the mismatch function, ϕ, is based on the prior information and the likelihood function, as in Sec. 2.2. For broadband data recorded at R ranges with errors that are uncorrelated in both frequency and space (range), assuming that the errors are random and Gaussian distributed, the likelihood function is given by

$$L(\mathbf{m}) = \prod_{r=1}^{R} \frac{1}{(\pi\nu_r)^N} \exp[-|\mathbf{d}_r^{obs} - \mathbf{d}_r(\mathbf{m})|^2/\nu_r]. \tag{2.25}$$

where $\mathbf{d}_r$ is a vector of acoustic data recorded at the r^{th} range over N frequencies. This expression inherently assumes that all data at the r^{th} range have the same variance.

Unfortunately, Eqn. 2.25 is not appropriate for the present case because the quantity $\mathbf{d}_r^{obs} - \mathbf{d}_r(\mathbf{m})$ requires an accurate knowledge of the calibrations and positions of the individual sensors. Since these were not known accurately it is assumed that the modelled data take the following form

$$\mathbf{d}_r(\mathbf{m}) = A_r e^{i\theta_r} \mathbf{d}_r^M(\mathbf{m}), \tag{2.26}$$

where $\mathbf{d}_r^M(\mathbf{m})$ is the acoustic field computed by the propagation model and $A_r e^{i\theta_r}$ represents the unknown array response (magnitude and phase) for a sensor at the r^{th} range. Substituting this expression into Eqn. 2.25 and setting $\partial L/\partial A_r = \partial L/\partial \theta_r = 0$ results in the following misfit function

$$E(\mathbf{m}) = \sum_{r=1}^{R} \frac{B_r(\mathbf{m})|\mathbf{d}_r^{obs}|^2}{\nu_r}. \tag{2.27}$$

In Eqn. 2.27 the quantity $B_r(\mathbf{m})$ represents the normalized Bartlett mismatch over frequency at the r^{th} range defined as

$$B_r(\mathbf{m}) = 1 - \frac{|\mathbf{d}_r^M(\mathbf{m})^\dagger \mathbf{d}_r^{obs}|^2}{|\mathbf{d}_r^M(\mathbf{m})|^2 |\mathbf{d}_r^{obs}|^2}. \tag{2.28}$$

These equations assume that the relative magnitude and phase are known across frequency at a single sensor. In this thesis it is assumed that the error variance is

the same at each sensor and at each frequency; therefore, the quantity $|\mathbf{d}_r^{obs}|^2/\nu_r$ in Eqn. 2.27 is constant.

In most cases, an estimate of the variance (ν) is not readily available which means that Eqn. 2.27 can not be utilized. Gerstoft and Mecklenbräuker (1998) estimated the variance by setting $\partial L/\partial \nu = 0$ and evaluating the result at the maximum likelihood estimate ($\mathbf{m}^{ML}$). In this work the same approach is employed and the expression of the variance is given by

$$\nu^{ML} = \frac{B(\mathbf{m}^{ML})|\mathbf{d}^{obs}|^2}{N_f}, \tag{2.29}$$

where N_f is the number of frequencies. The maximum likelihood estimate is obtained by minimizing the objective function

$$\phi(\mathbf{m}) = \sum_{r=1}^{R} B_r(\mathbf{m}), \tag{2.30}$$

using an optimization algorithm such as described in Sec. 2.3.

The above formulation assumes that there are independent errors at each of the sensors. However, for an array the errors can be correlated from sensor to sensor. Gerstoft and Mecklenbräuker (1998) suggest using an estimate of the number of uncorrelated sensors N_e, where $N_e < N_f$, and took N_e to be the number of propagating modes. In this thesis it is assumed that the errors at all frequencies and sensors are uncorrelated.

It is often constructive to define an effective signal-to-noise ratio (ESNR) to compare the "signal" to all sources of error (measurement and theory) not just to the ambient noise in the environment. Dosso and Nielsen (2002) derived the following expression for ESNR

$$ESNR = 10\log\left[\frac{1 - B(\mathbf{m}^{ML})}{B(\mathbf{m}^{ML})}\right], \tag{2.31}$$

where $B(\mathbf{m}^{ML})$ is the Bartlett mismatch for the maximum likelihood estimate.

2.6 Acoustic Propagation Models

The previous section described MFI which is a forward modelling approach to geoacoustic inversion and requires an accurate acoustic propagation model. Four types of acoustic propagation models are commonly used:

1) ray-based models,

2) normal mode models,

3) parabolic equation models, and

4) wave number integral models.

For the work in this thesis the first three propagation models were used and are briefly discussed below.

2.6.1 Ray Theory Model: GAMARAY

Most of the inversions carried out in this work used the ray theory model GAMARAY (Westwood & Vidmar, 1987; Westwood & Tindle, 1987). GAMARAY is a broad-band propagation model that employs ray theory to predict acoustic fields for range-independent, layered-bottom ocean environments. The model computes the travel time, phase shift, frequency-dependent attenuation, reflection and transmission loss, and spreading loss for each eigenray. GAMARAY was employed because there was a need to compute broad-band acoustic fields for close ranges ($\leq$ 500 m) in an efficient manner.

To date ray theory models have not been used extensively for geoacoustic inversion. Pignot and Chapman (2001) matched travel times and magnitudes of ray arrivals at a VA to estimate geoacoustic properties of a range-dependent environment. Chapman et al. (2002) successfully applied GAMARAY to invert time-domain data in

the 300-1000 Hz band. Park et al. (2003) inverted high-frequency towed array data using a simple ray model.

F=aaG Bk

2.6.2 Normal-mode Model: ORCA

The normal-mode propagation model ORCA (Westwood, Tindle, & Chapman, 1996) was used for the investigation of algorithm-induced variability described in Chapter 4. ORCA makes use of the reflection coefficients from upward- and downward-travelling plane waves. The algorithm for finding the eigenvalues is formulated in terms of the product of the two reflection coefficients. The plane wave reflection coefficient calculations provide the ability to include elastic layers above and below the ocean. Once the mode eigenvalues have been calculated, the compressional and shear mode functions are determined from the wave equation solutions in each layer. The solutions for the wave equation are obtained during the process of computing the plane wave reflection coefficients.

ORCA was also employed to benchmark the inversions using GAMARAY. To date ORCA has been used extensively for geoacoustic inversion problems and has been widely accepted as a standard propagation model for this problem. However, GAMARAY has not been used as often and has yet to be proven for geoacoustic inversion problems, especially at lower frequencies. To ensure the robustness of the inversions a careful comparison of GAMARAY and ORCA was conducted. This required adjusting many of the internal settings (e.g., number of ray paths, number of internal reflections within a layer and the cut-off dB level) used in GAMARAY to make the model produce more precise acoustic fields. This also included turning off the beam displacement and caustic calculations. In general low mismatches, on the order of 10^{-3}, could be achieved. A comparison of inversion results for the two models was carried out by Fallat et al. (2002). Although that study did not directly compare the output of

the models it did show that the results were in good agreement within the expected variability of the inversion.

2.6.3 Parabolic Equation Model: RAMGEO

RAMGEO (Collins, 1993, 1994) is used for the generation of synthetic range-dependent data which are inverted in Chapter 5. RAMGEO is a parabolic equation model based on a split-step Padé solution. Parabolic equation models are useful because they can provide accurate estimates of acoustic propagation in both range-independent and range-dependent environments. The drawback is that for MFI the method is computationally intensive.

Chapter 3

Experiments

In this thesis acoustic data from two experiments are analyzed. The first experiment was conducted in the spring of 2000 and is known as MAPEX 2000. The second experiment was BOUNDARY 2003 which was conducted in July, 2003. Both experiments were carried out in the Strait of Sicily, Mediterranean Sea (Fig. 3.1). These experiments offer an excellent opportunity to evaluate data recorded at the same location using different experimental setups. In particular, the experiments used arrays with significantly different lengths, hydrophone spacing and source frequencies.

3.1 MAPEX 2000 Experiment

The MAPEX 2000 experiment (Siderius et al., 2002; Fallat, Nielsen, Dosso, & Siderius, 2005b) had several objectives, one of which was to test the effectiveness of characterizing a range-dependent environment using towed horizontal array data. The ship track for the portion of the MAPEX 2000 experiment considered here is shown in Fig. 3.2. Two course deviations were required to avoid a fishing vessel (northern deviation) and a moored vertical array (southern deviation). During the

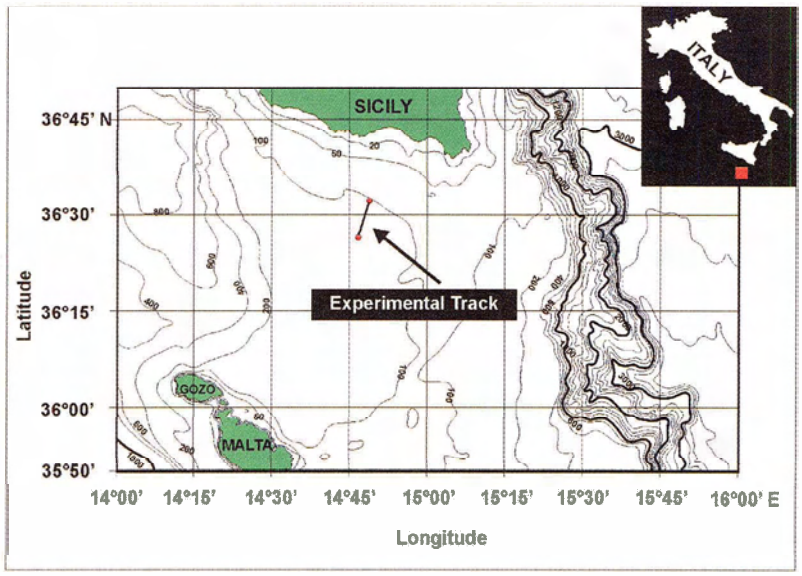

Figure 3.1: Site of the MAPEX 2000 and BOUNDARY 2003 experiments.

course deviations the resulting deformation of the towed array meant that fewer or no inversions could be carried out.

Sound speed profiles (Fig. 3.3) were measured during the experiment using a conductivity, temperature and depth (CTD) probe and expendable bathythermograph (XBT) sensors. The measurements were taken before, during and after the acoustic data were recorded at various positions along the track and showed little temporal and spatial variation. The sound-speed profiles were weakly upward refracting which is typical for this area of the Mediterranean Sea in the spring (Caiti et al., 1996; Siderius et al., 2002).

Bathymetry measurements at the time of each acoustic ping were provided by a multi-beam echosounder mounted on the bottom of the ship and are shown in Fig. 3.4. Depth measurements for the source and the array were provided by pressure sensors and are shown in Fig. 3.5. The array included depth sensors at the head and tail and the values shown in Fig. 3.5 are the average of these measurements. The depth

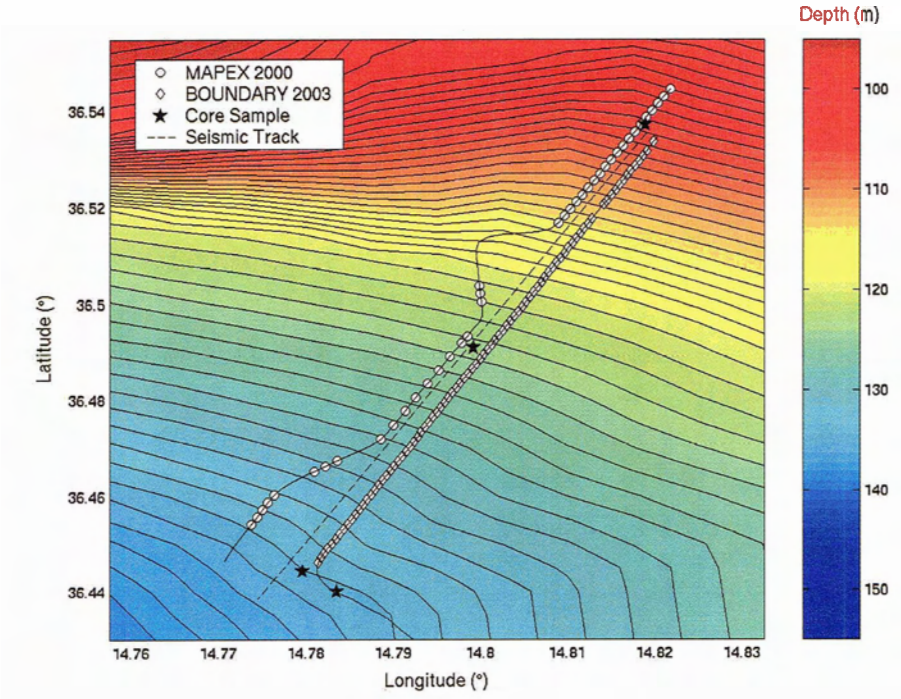

Figure 3.2: Ship tracks for the MAPEX 2000 and BOUNDARY 2003 experiments. Also included are the locations of several core samples and a track for the high-resolution seismic profile. The circles and diamonds are the locations where inversions were carried out.

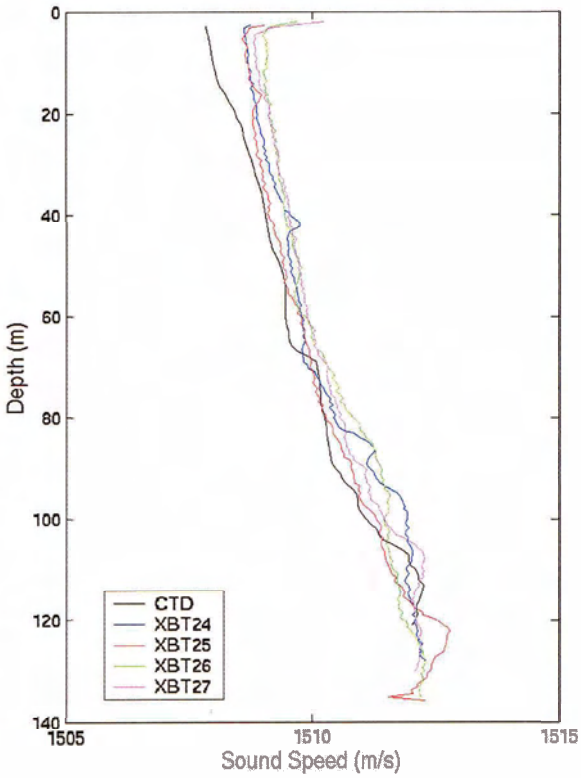

Figure 3.3: Sound speed profile from CTD and XBT casts taken during the MAPEX 2000 experiment.

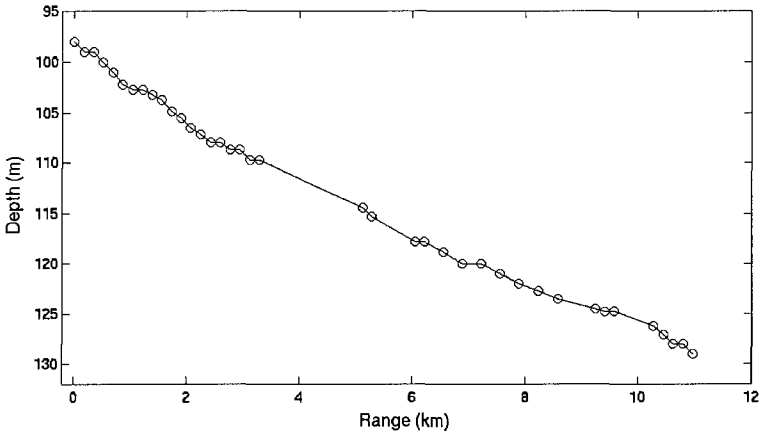

Figure 3.4: Multi-beam echosounder measurements for the MAPEX 2000 track.

measurements showed that the array had an average tilt of $\sim 1°$. The array contained 64 sensors spaced 4 m apart for a total acoustic aperture of 252 m [see Fig. 3.6 a)]. The source and array were separated by $\sim$ 300 m resulting in a maximum range of approximately 550 m.

The range of grazing angles covered by the HA at each end of the experimental track is given in Table 3.1. Note that the water depths at the Northern and Southern ends of the track were 97 and 129 m respectively which resulted in a different range of grazing angels begin covered by the HA. Investigating the range of grazing angles covered by the HA can provide useful insight into what geoacoustic properties are expected to be resolvable in the inversions. Below the critical angle attenuation typically has an influence on the propagating field while above the critical angle it is changes in the density that influence the propagation. The sound speed in the bottom can have an influence on the propagating field at all grazing angles (Jensen, Kuperman, Porter, & Schmidt, 1994) with the most profound effect occurring near the critical angle. For this experimental setup a wide range of grazing angles is covered, therefore it is expected that the inversions should be sensitive to the geoacoustic

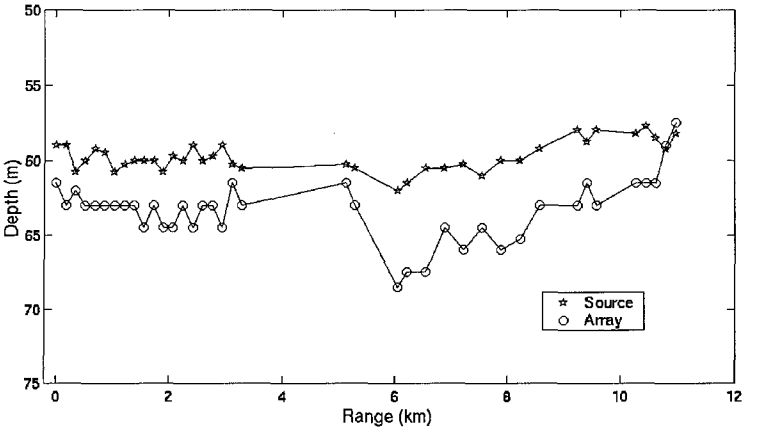

Figure 3.5: Depth measurements for source and array for the MAPEX 2000 experiment.

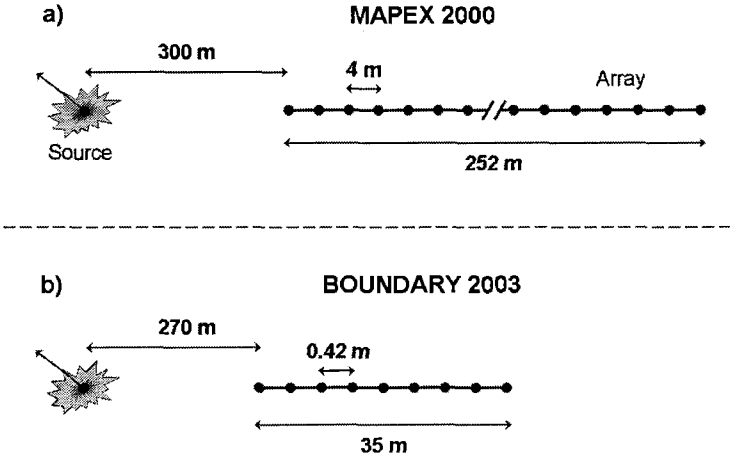

Figure 3.6: Schematic diagrams of the array setup for the MAPEX 2000 (a) and BOUNDARY 2003 (b) experiments.

Table 3.1: Range of grazing angles for the MAPEX 2000 experimental setup for three dominant bottom interacting ray paths.

Ray Path	Northern End	Southern End
Bottom	7.5° – 14°	14° – 25°
Surface-Bottom	19° – 33°	25° – 41°
Bottom-Surface-Bottom	26° – 42°	36° – 53°

properties.

The flextensional source produced a 1-s linear frequency modulated sweep from 150–800 Hz. The signals were repeated every minute which, with a ship speed of 5 knots, resulted in a 150 m spacing between transmissions. Figure 3.7 shows an example of the recorded time series and the corresponding power spectrum. The acoustic data recorded at the array were calibrated by dividing a measured source spectrum over the source frequency band. The source spectrum was recorded prior to the experiment using a reference hydrophone located 2 m from the (stationary) source in the middle of the water column (water depth $>$ 100 m). The matched filtered response across the array, for a data set at the southern end of the track, is shown in Fig. 3.8. Included in the figure is an explanation of the most significant arrivals (i.e., direct blast, first surface and bottom bounce and the arrival from the first sediment layer interface). After matched filtering the band-limited pulse width is 0.0015 s.

3.2 BOUNDARY 2003 Experiment

The BOUNDARY 2003 experiment was part of a series of experiments focused on characterizing the effects of the interaction of low to mid-frequency sound with the sea floor and sea surface. Figure 3.2 shows the BOUNDARY 2003 ship track that

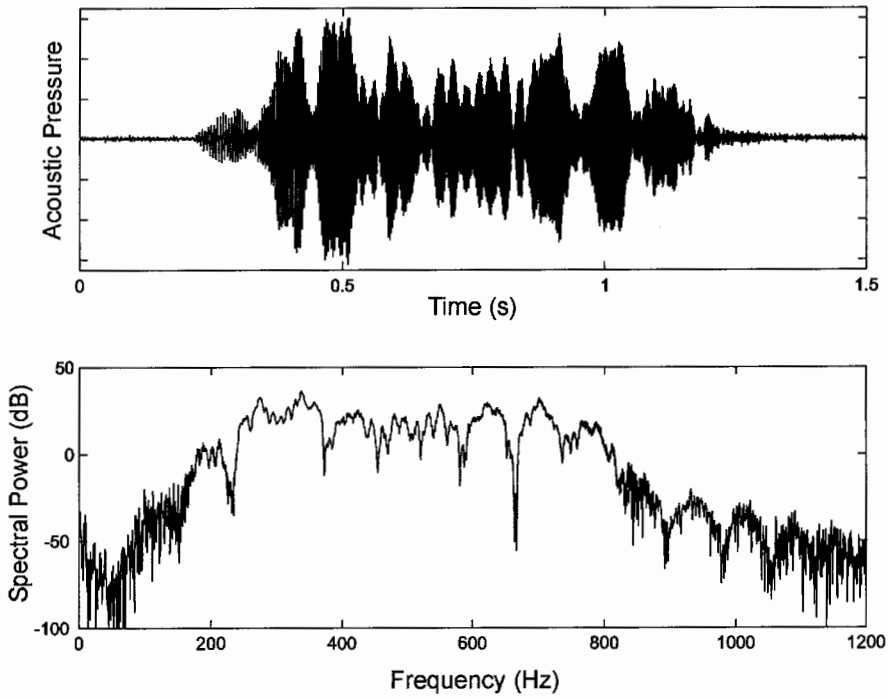

Figure 3.7: Example of recorded times series and the corresponding power spectrum for the MAPEX 2000 data. The acoustic pressure was in arbitrary dB units.

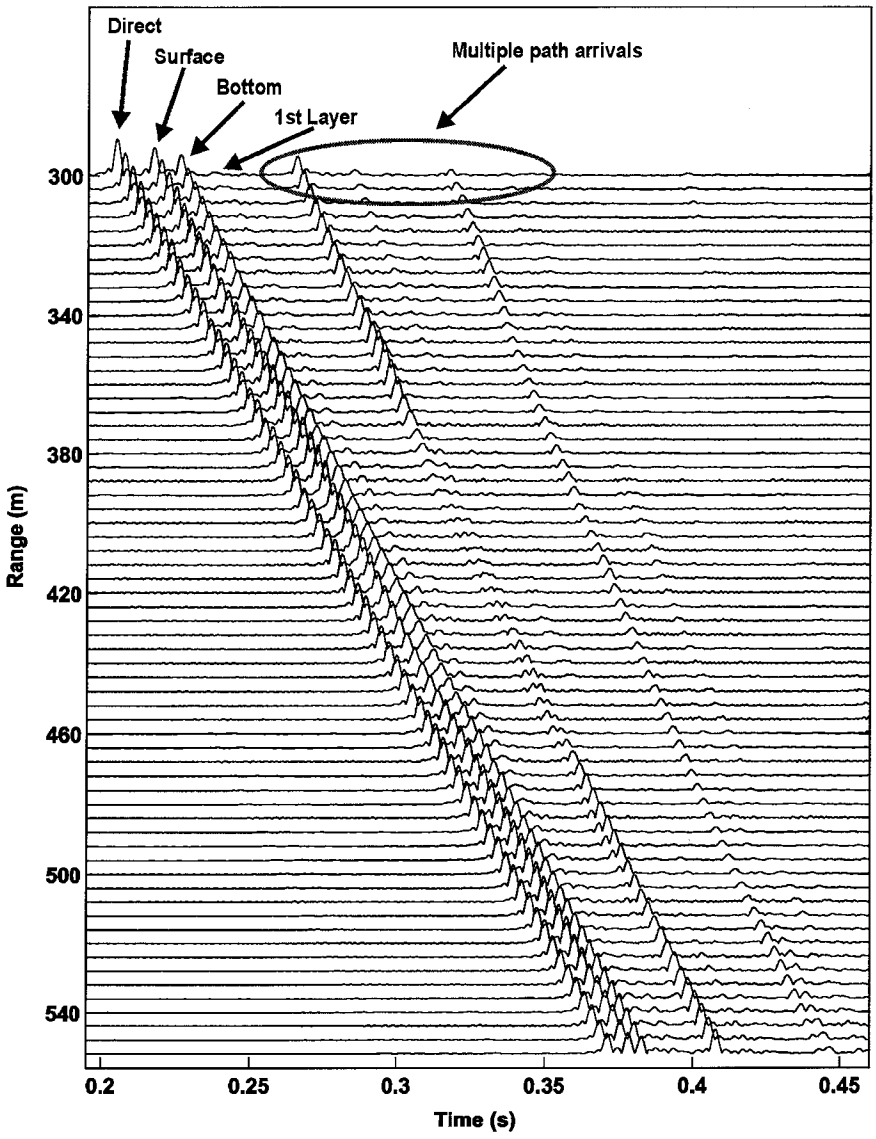

Figure 3.8: The matched filtered response for one ping of MAPEX 2000 data. The "1^{st} layer" refers to the arrival from the bottom of the first sediment layer.

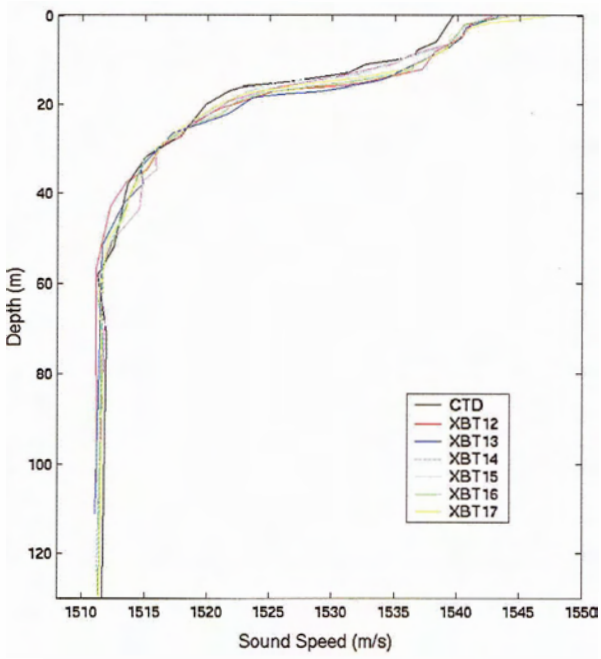

Figure 3.9: Sound speed profiles from CTD and XBT casts taken during the BOUNDARY 2003 experiment.

was used for this work.

As with the MAPEX 2000 experiment, sound speed profiles were measured before during and after the acoustic data were recorded using CTD and XBT sensors. The sound speed measurements are shown in Fig. 3.9 and illustrate a strong downward refracting layer to a depth of approximately 50 m over an iso-speed layer. These are significantly different from the profiles recorded during the MAPEX 2000 experiment (see Fig. 3.3) because high temperatures in the summer of 2003 resulted in significant surface heating.

For the BOUNDARY 2003 experiment a free-flood ring transducer was used as a source. Before the experiment was conducted an evaluation of the source was carried

out by placing a vertical array very close to the source (< 10 m) in approximately 200 m of water. The purpose of this was to determine the extent of the beam pattern and to record a source spectrum for calibrating the data. Figure 3.10 shows the measured beam pattern, averaged over the frequency band, is quite flat with a variation of less than 2 dB. Note that the beam pattern is not centred, because the source was not exactly perpendicular to the array.

The source produced 1-s, linear frequency modulated sweeps from 750–2000 Hz. The same coverage as in the MAPEX 2000 experiment was also used for BOUNDARY 2003 (i.e., signals transmitted every minute, ship speed of 5 knots). The recorded time series and the corresponding power spectrum are shown in Fig. 3.11. The matched filtered response across the array is shown in Fig. 3.12. In this case, the band-limited pulse width after matched filtering is 0.0008 s.

Figure 3.13 shows the source and array depths recorded during the experiment. Again, the array depth represents the average between the head and tail depth-sensor measurements. The average tilt of the array was 1°. The array consisted of 84 sensors spaced 0.42 m apart for a total length of slightly less than 35 m [see Fig. 3.6 b)]. The array was towed behind the ship at a nominal distance of 270 m. Finally, the measured bathymetry for the BOUNDARY 2003 experiment is shown in Fig. 3.14.

The range of grazing angles covered by the HA at each end of the experimental track is given in Table 3.2. Although the total range of angles covered by this array is somewhat similar to the array used in the MAPEX 2000 experiment there are significant gaps that may cause some difficulties in the inversion.

3.3 Environmental Data

This particular experimental site was chosen, in part, because there have been several other experiments conducted in the area. Of interest here is some of the environmental

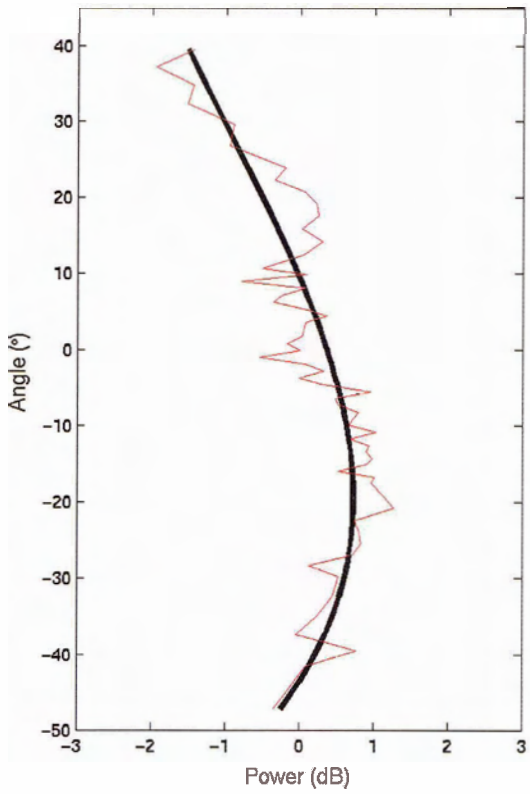

Figure 3.10: Measured beam pattern of the middle pair of rings for the BOUNDARY 2003 source. The red line are the actual measurements and the black line is a third order polynomial fit to the data.

Table 3.2: Range of grazing angles for the BOUNDARY 2003 experimental setup for three dominant bottom interacting ray paths.

Ray Path	Northern End	Southern End
Bottom	$14° - 15°$	$24° - 27°$
Surface-Bottom	$32.5° - 36°$	$40° - 44°$
Bottom-Surface-Bottom	$41° - 45°$	$52° - 56°$

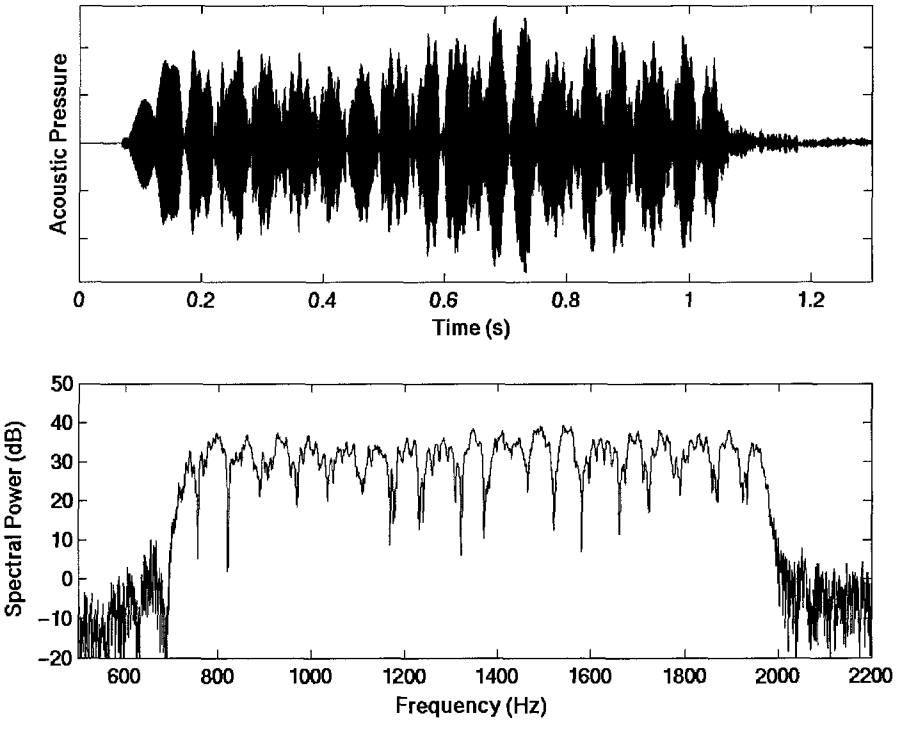

Figure 3.11: Example of recorded times series and the corresponding power spectrum for the BOUNDARY 2003 data. The acoustic pressure was in arbitrary dB units.

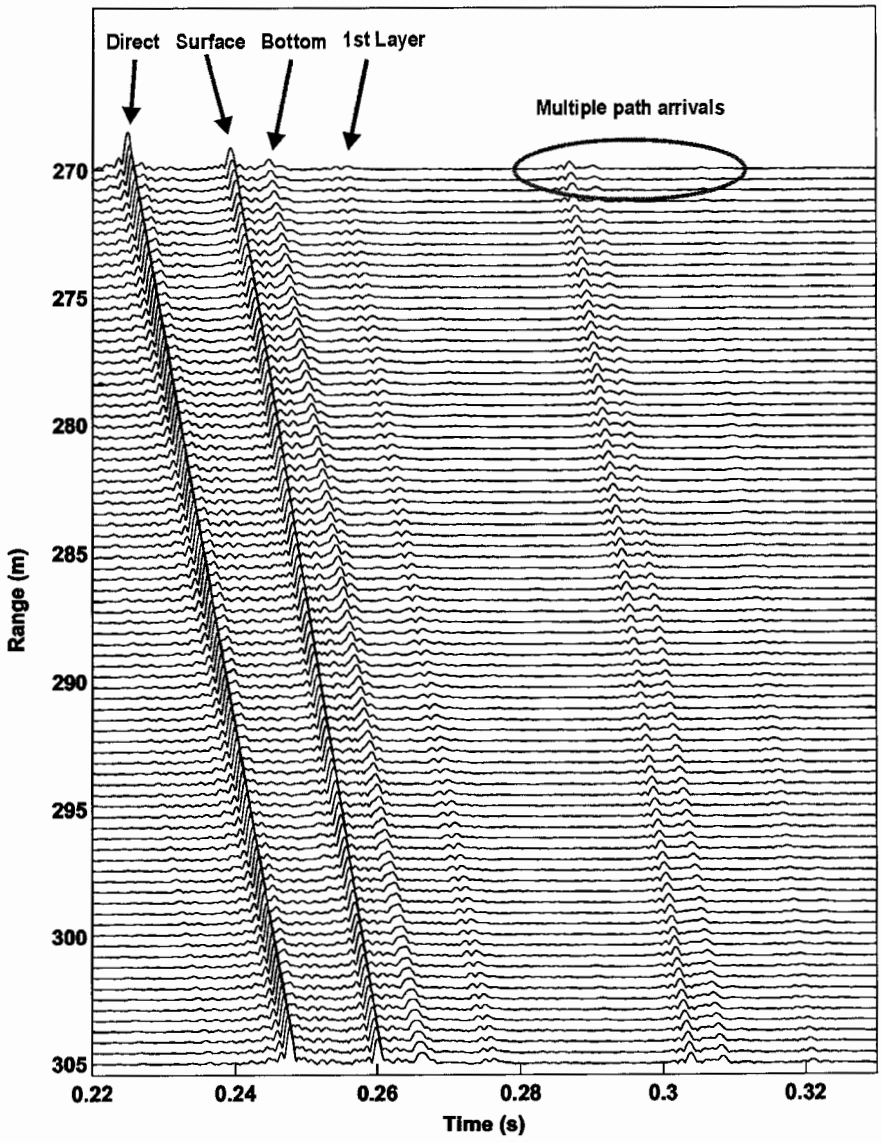

Figure 3.12: The matched filtered response for one ping of BOUNDARY 2003 data. The "1^{st} layer" refers to the arrival from the bottom of the first sediment layer.

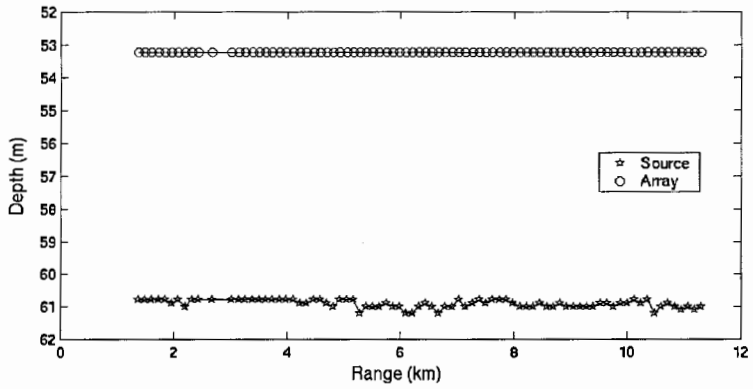

Figure 3.13: Depth measurements for the source and the array for the BOUNDARY 2003 experiment.

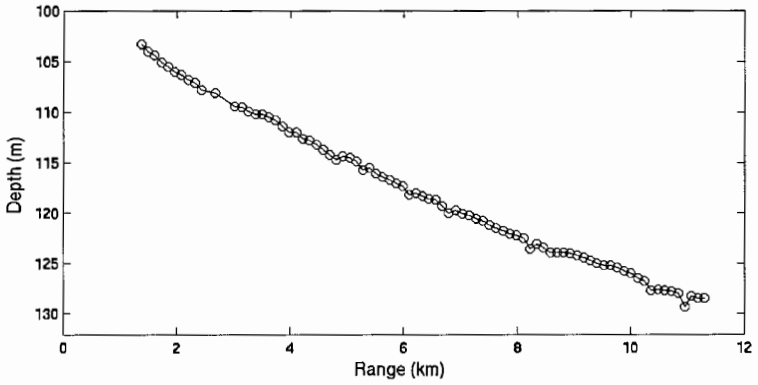

Figure 3.14: Multi-beam echosounder measurements for the BOUNDARY 2003 track.

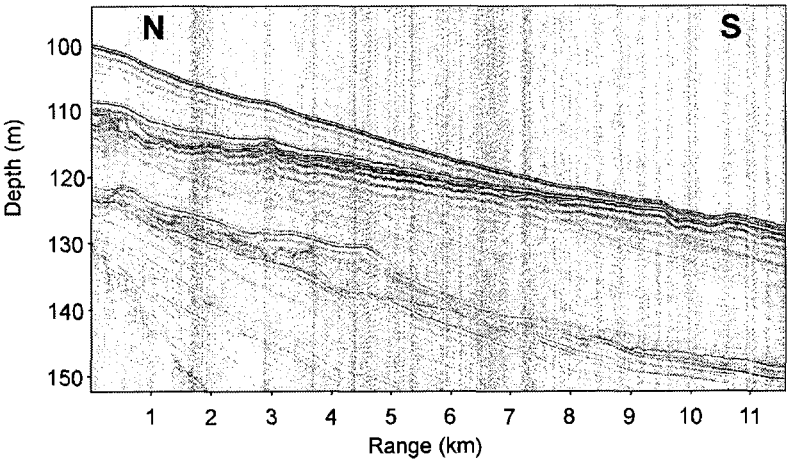

Figure 3.15: High resolution seismic profile from the experimental site.

data collected during these other experiments, particularly core and seismic data. Included in Fig. 3.2 is the track of the high-resolution seismic profile shown in Fig. 3.15 (Osler & Algan, 1999). The profile was obtained using a boomer source (center frequency: 6 kHz) and a single-channel towed array of 10 hydrophones which was 2 m in length. Figure 3.15 indicates three well defined reflectors out to a range of approximately 8 km. The first reflector is the water-sediment interface. The second reflector represents the bottom of a low-speed sediment inclusion (Osler & Algan, 1999; Siderius et al., 2002) which gets thinner with range and pinches out around 8–9 km. The third reflector has a relatively constant separation of $\sim$ 20 m from the water-sediment interface, and is taken to represent the acoustic basement, although there is the suggestion of a deeper layer out to 4-km range.

Figure 3.2 also shows the locations of four shallow core samples which were collected in the area. Figure 3.16 shows the sound speeds and densities estimated from these cores. The data have been grouped into two categories; the northern (northmost and middle) and the southern cores. There is a noticeable difference between the northern and southern cores, especially as the depth increases. The northern cores

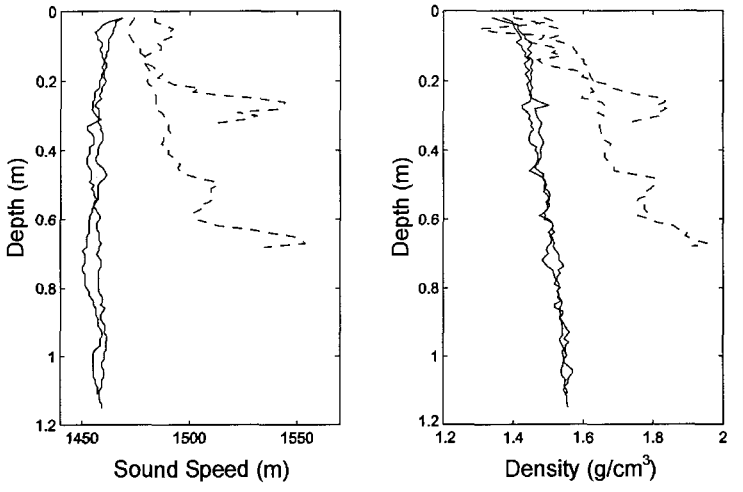

Figure 3.16: Core samples from the experimental region showing estimates of the sound speed and density of the surficial sediments. The solid lines represent the two northern cores while the dashed lines represent the southern cores.

show much less variation with depth than the southern cores and indicate a uniform sound speed of approximately 1460 m/s to a maximum penetration depth of 1.2 m. These core locations correspond to the inclusion shown in the seismic profile. The southern cores only penetrated approximately 0.5 m due to the more consolidated nature of the sediments. For these cores, which correspond to locations where the inclusion is absent, the measured sound speed increases with depth from about 1480 m/s at the seafloor to $\sim$ 1550 m/s. Since the sound speed at greater depths is likely to be at least this high, a sound speed of 1550 m/s is adopted for comparison with the inversion results. In simple terms, the cores showed that the northern end of the track had a soft bottom with a sound speed lower than the water column while the southern end had a harder bottom with a sound speed greater than the water.

The densities are shown in the right panel (Fig. 3.2) and also showed two different sediment types. The northern cores had a fairly constant density with depth that was

lower than the southern cores with an average value of 1.49 g/cm^3. The southern cores showed more variation as a function of depth than the northern cores. As with the sound speed, the value at the bottom of the core (1.82 g/cm^3) was assumed to be representative of the density of the upper most sediments at this site.

Chapter 4

Variability in Inversion Algorithms

4.1 Introduction

A variety of search algorithms have been applied to the geoacoustic MFI, including global optimization methods such as simulated annealing (SA) and its variants (Collins et al., 1992; Dosso et al., 1993; Lindsay & Chapman, 1993; Collins & Fishman, 1995) genetic algorithms (GA) (Gerstoft, 1994; Heard et al., 1998; Siderius et al., 1998) as well as hybrid methods (Gerstoft, 1995; Fallat & Dosso, 1999; Musil et al., 1999; Dosso et al., 2001). Recently, two major workshops with accompanying special journal issues (Chapman et al., 1998, 2003), have been dedicated specifically to investigating and comparing MFI algorithms using noise-free synthetic data.

Geoacoustic inversion methods have been applied to assess temporal and spatial variability in the environment. For example, Siderius et al. (2001) and Snellen et al. (2001) considered geoacoustic inversion of vertical array data along a fixed path over a period of hours, and interpreted the variability in the inversion results in terms of sensitivity to temporal variations in the ocean sound-speed profile. Siderius et al. (2002) and Fallat et al. (2005b) considered the variability of inversion results for

towed array data in terms of spatially-varying seabed structure along the tow track.

Before conclusions on temporal or spatial variations can be drawn from MFI results, however, it is important to consider the variability inherent in the inversion procedure itself, i.e., the repeatability or consistency of results simply due to the different random initializations of the algorithm. Snellen et al. (2001) investigated this by carrying out multiple GA inversions of (noise-free) simulated data. However, the actual variability in inversion results can vary considerably between simulated data (noise-free and noisy) and measured data, and can also be a function of the inversion algorithm applied.

This chapter investigates the variability of three geoacoustic inversion algorithms for noise-free and noisy synthetic data from the 1997 Geoacoustic Inversion Workshop (Chapman et al., 1998) and for measured data from the MAPEX 2000 experiment. The algorithms considered are GA (Gerstoft, 1994, 1995; Sen & Stoffa, 1995), a variant of fast simulated annealing (FSA) (Szu & Hartley, 1987; Liu et al., 1995; Fallat & Dosso, 1998), and a hybrid inversion algorithm, adaptive simplex simulated annealing (ASSA) (Fallat & Dosso, 1999; Dosso et al., 2001). In particular, this chapter seeks to determine which algorithm induces the least variability so that it can be used for the work in the subsequent chapters. The contents of this chapter have already appeared in a published journal article by Fallat et al. (2004).

Although the main goal of this thesis is the inversion of HA data, in this chapter both HA and VA data are considered. This was done for several reasons. First, several recent papers have interpreted the variability of VA inversions in terms of temporal or spatial variation in the environment. These studies have not fully considered the importance of variability in the inversion algorithm. Second, geoacoustic inversion has more commonly been applied to VA data than HA data, and it is clearly of interest to examine the reliability of inversion algorithms for both cases. Finally, it is common practice to evaluate optimization algorithms on problems other than

solely the application at hand in order to draw more general conclusions. For example, arbitrary mathematical functions have been used to test geoacoustic inversion algorithms (Musil et al., 1999; Fallat & Dosso, 1999; Dosso et al., 2001; vanMoll & Simons, 2004). The conclusions of the analysis in this chapter are the same for both HA and VA data: ASSA provides the least algorithm-induced variability; however, even with ASSA this variability is not necessarily negligible and must be considered on a case-by-case basis.

4.2 Synthetic Data Inversions

In this section, the three algorithms are evaluated using a synthetic testcase developed for the 1997 Matched Field Workshop (Chapman et al., 1998). The testcase involved determining the geometric and geoacoustic parameters for the environment shown in Fig. 4.1 where the form of the geoacoustic model was known to consist of a sediment layer over a semi-infinite basement. The inversions involved nine unknown parameters including the water depth, D, source range and depth, r and z, sediment thickness, h, sound speeds at the top and bottom of the sediment layer, c_0 and c_1 (linear gradient assumed), sound speed in the basement, c_2, and densities in the sediment and basement, ρ_s and ρ_b, respectively.

The data used here consist of complex acoustic pressures at frequencies of 200–500 Hz in 50 Hz increments recorded at a vertical array of 40 hydrophones spanning $\sim 2/3$ of the 115 m water column. Data and the replica fields were generated using the normal mode code ORCA (Westwood et al., 1996). The data fields were generated by the author using the property values provided in the Workshop paper (Chapman et al., 1998). The objective function used for the synthetic data inversions was based on the Bartlett processor coherent in depth and summed incoherently in frequency (normalized to [0,1]). The evaluation of the algorithms involved both noise-free and noisy

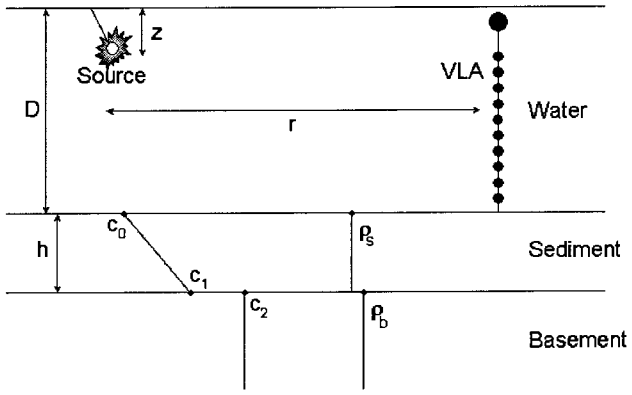

Figure 4.1: Schematic diagram of the ocean environment used for the synthetic data inversions.

realizations of the synthetic data. For each data set several independent inversions were carried out to assess variability in the results. The independent inversions were obtained by running the algorithms with different random starting models, different annealing schedules and for GA different discretizations for the parameter search intervals.

4.2.1 Noise-free Data

Figure 4.2 shows the inversion results for ASSA, GA and FSA for the noise-free synthetic data. For each algorithm, four independent inversions were carried out and the results displayed represent the model that obtained the lowest objective function value in each inversion.

The results from ASSA are consistently in excellent agreement with the true values for all parameters, i.e., show essentially no variability. The GA results show

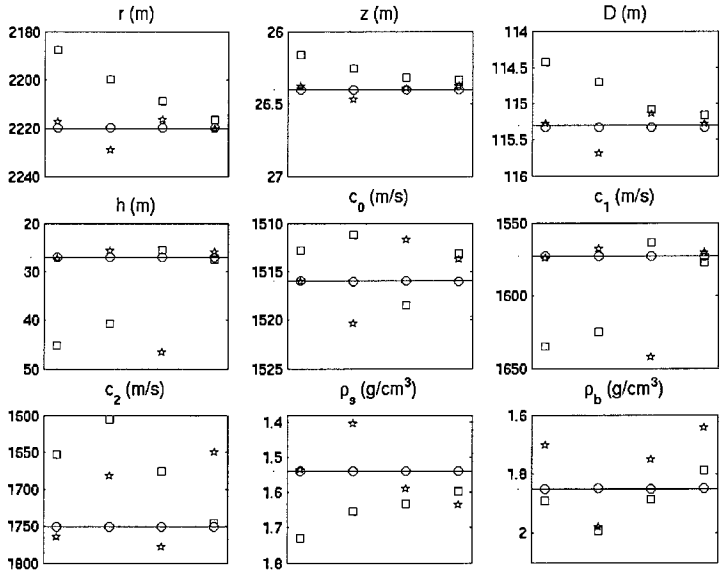

Figure 4.2: Inversion results for the noise-free testcase. The inversion results for ASSA are represented by circles, for GA by stars and for FSA by squares. The solid line in each panel represents the true parameter value.

significantly more variability about the true parameter values. One of the final models does approximate the true parameter values quite well with the exception of the basement density. Finally, the inversion results for FSA are the poorest of the three, although reasonable parameter values are obtained for at least one inversion. The final, best objective function values were 1.8×10^{-10} for ASSA, 2.8×10^{-4} for GA and 6.5×10^{-3} for FSA. Table 4.1 summarizes the best inversion result for the three algorithms.

The outliers in h and c_1 that occur in the GA and FSA results in Fig. 4.2 can be explained in terms of a (positive) correlation between these two parameters. Figure 4.3 shows a 2-D cross section of the objective function versus h and c_1 (all other para-

Table 4.1: Summary of the best inversion results for the noise-free testcase.

	D (m)	r (m)	z (m)	h (m)	c_0 (m/s)	c_1 (m/s)	c_2 (m/s)	ρ_s (g/cm^3)	ρ_b (g/cm^3)
True	115.33	2220	26.40	27.08	1516.0	1573.0	1751.0	1.54	1.85
ASSA	115.33	2220	26.40	27.08	1516.0	1573.0	1751.0	1.54	1.85
GA	115.28	2217	26.38	27.32	1516.1	1574.3	1764.7	1.54	1.70
FSA	115.69	2209	26.32	25.62	1518.5	1563.9	1675.7	1.63	1.89

meters held at true values). This figure illustrates the correlation, which is characterized by narrow oblique valleys intersected by local minima. The correlation for this testcase has been discussed previously (Fallat & Dosso, 1999; Dosso, 2002), and has also been observed for experimental data (Fallat et al., 2000; Dosso & Nielsen, 2002). A weak positive correlation also exists between r and D. It should be noted that ASSA overcomes these correlations because it is sensitive to the multi-dimensional gradient information through the local component of the algorithm (DHS).

The relative sensitivity of the parameters in this benchmark problem have been discussed at length in a number of previous works (Heard et al., 1998; Fallat & Dosso, 1999; Chapman et al., 1998; Fallat & Dosso, 1998). Essentially, the geometric parameters have the highest sensitivity, followed by sound speeds and layer thicknesses, with densities of lowest sensitivity.

4.2.2 Noisy Data

Although the 1997 Workshop utilized noise-free data, to provide a more realistic evaluation of the inversion algorithms, Gaussian noise was added to the data. For these inversions, five different noise realizations with a signal to noise ratio of 10 dB at each frequency were generated. This has been found to represent a realistic level

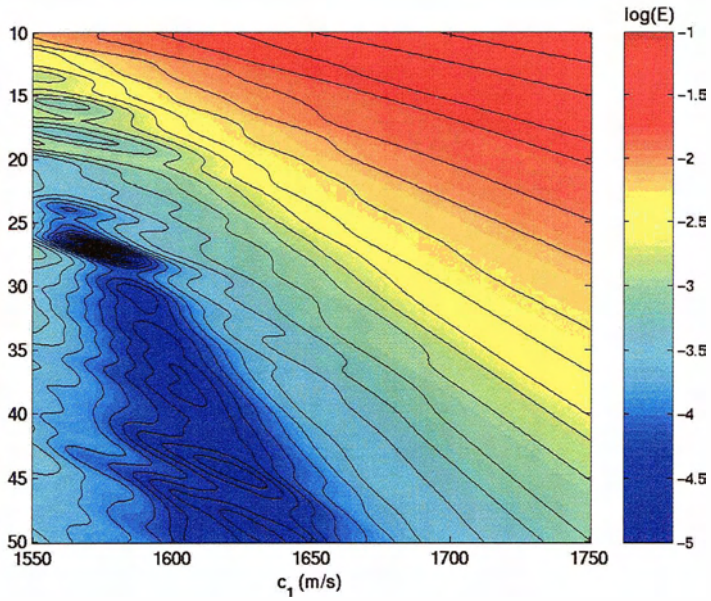

Figure 4.3: 2-D cross section of $\log(E)$ versus h and c_1, illustrating the strong correlation between these parameters.

of noise (including experimental mismatch, see Eqn. 2.31) (Dosso & Nielsen, 2002). To assess the variability of the results, six independent inversions were carried out with each algorithm for each noise realization.

Figure 4.4 shows the objective function values obtained for the inversions. The plots have been truncated to better demonstrate the differences in the objective function values; therefore, some of the FSA results with higher objective function values are not included. Also, some of the GA inversions obtained very similar objective function values using the same number of forward model evaluations and are plotted essentially on top of each other. ASSA obtained the lowest objective function values for most inversions (80%). Figure 4.4 shows that ASSA and GA both obtained lower objective functions values than FSA in all but one case. For the first, second and fifth noise realizations, several of the inversions become trapped in a local minimum

with a slightly higher objective function value than for the true parameters (solid line). This local minimum will be discussed in greater detail later. Note also that in several instances ASSA obtained objective function values lower than that for the true parameters.

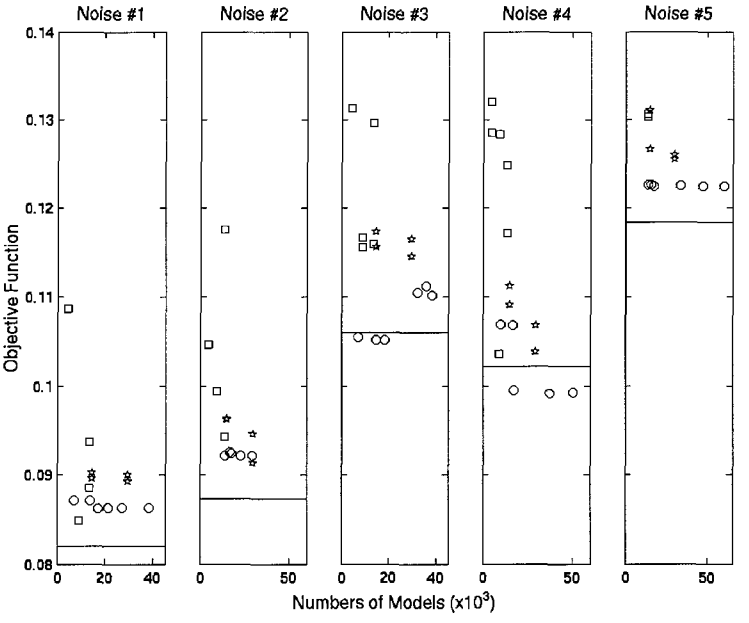

Figure 4.4: Objective function values as a function of the number of model calls for the three algorithms and for the five different noise realizations. The inversion results for ASSA are represented by the circles, for GA by the stars and for FSA by the squares. The solid lines represent the objective function value for the true parameters.

The inversion results for FSA, shown in Fig. 4.5, exhibit a large degree of variability within each noise realization. Particular models appear to approximate the true parameter values for some of the most sensitive parameters, but in general the results are unstable.

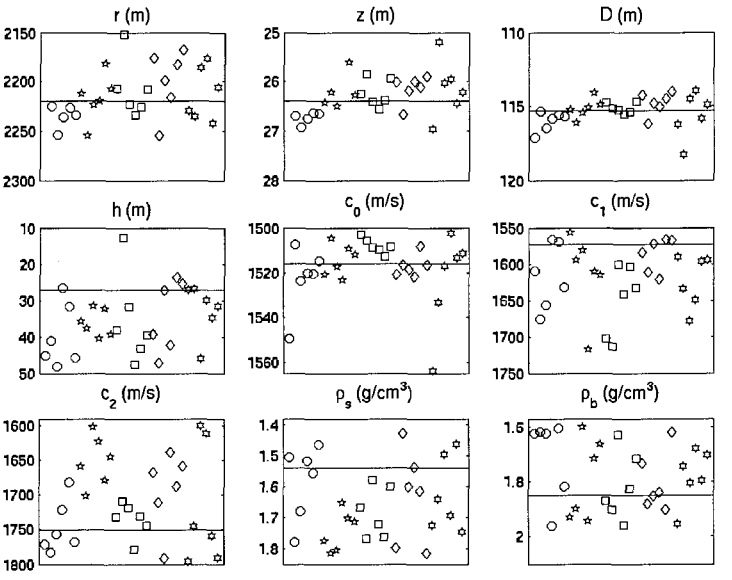

Figure 4.5: FSA inversion results of the noisy synthetic data. Each symbol represents a different noise realization (six independent inversions per noise realization). Solid lines represent the true parameter values.

Figure 4.6 shows the results obtained using ASSA. For most of the parameters the results are stable and closely approximate the true parameter value. However, the results for ρ_b appear essentially random (due to the low sensitivity for this parameter) and the results for h and c_1 indicate that ASSA is trapped in a local minimum.

To further investigate this local minimum, the models that ASSA accepted during inversions of the third noise realization are plotted in Fig. 4.7. This plot includes the models for two independent inversions, one that closely approximated the true sediment parameters and one that converged to the local minimum. This figure represents a projection of all models in the multidimensional space onto the particular parameter axis and can provide an impression of the overall multidimensional structure.

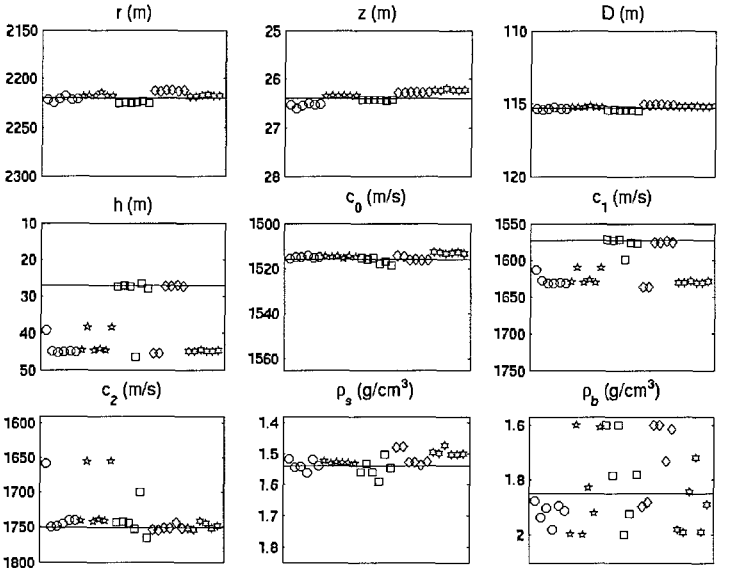

Figure 4.6: ASSA inversion results for noisy synthetic data. Each symbol represents a different noise realization (six independent inversions per noise realization). Solid lines represent the true parameter values.

Figure 4.7 clearly demonstrates two well defined minima, one close to the true parameter values ($h \sim 27$ m, $c_1 \sim 1572$ m/s) and a broader one at higher values ($h \sim 47$ m, $c_1 \sim 1600$ m/s). Note that the objective function values at the two minima are almost identical, and differ by only 0.006 (for E normalized between [0,1]), indicating the strong non-uniqueness of this problem.

The inversion results for GA are presented in Fig. 4.8. For several of the parameters the agreement is quite good but in general the results are not as stable as for ASSA (Fig. 4.6). GA appears to become trapped in the local minima associated with h and c_1 described above, although not as frequently as ASSA. However, the variability of results within a particular noise realization is generally larger for GA

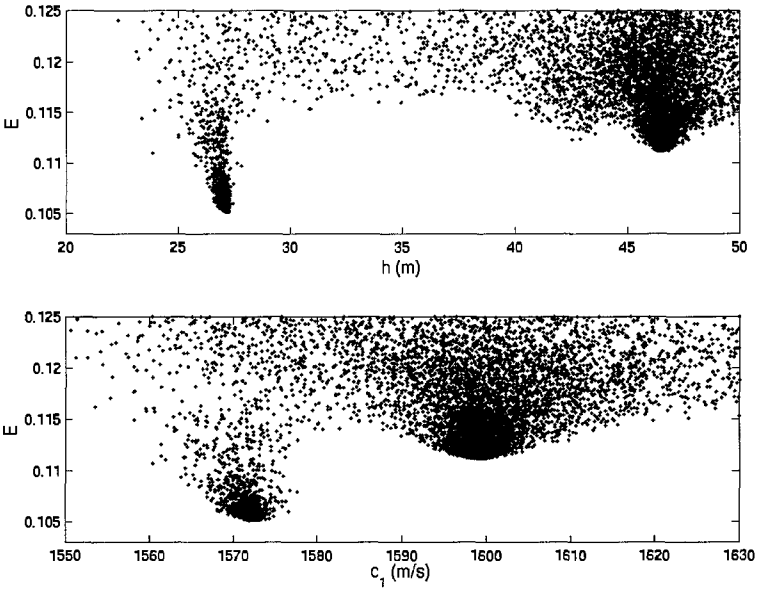

Figure 4.7: Objective function E versus sediment layer thickness and sound speed at the bottom of the sediment for two independent ASSA inversions of the third noise realization. The plot has been truncated at low objective function values to better demonstrate the structure of the minima.

than ASSA.

4.3 Experimental Data Inversions

This section applies the inversion algorithms to data from the MAPEX 2000 experiment (see Chapter 3). Since it was evident from the synthetic inversions that FSA was not particularly effective, this method is not included in the comparison.

Figure 4.9 shows the experimental setup and the environmental model used for the inversions. Previous studies (Siderius et al., 2002; Fallat et al., 2004) have shown that

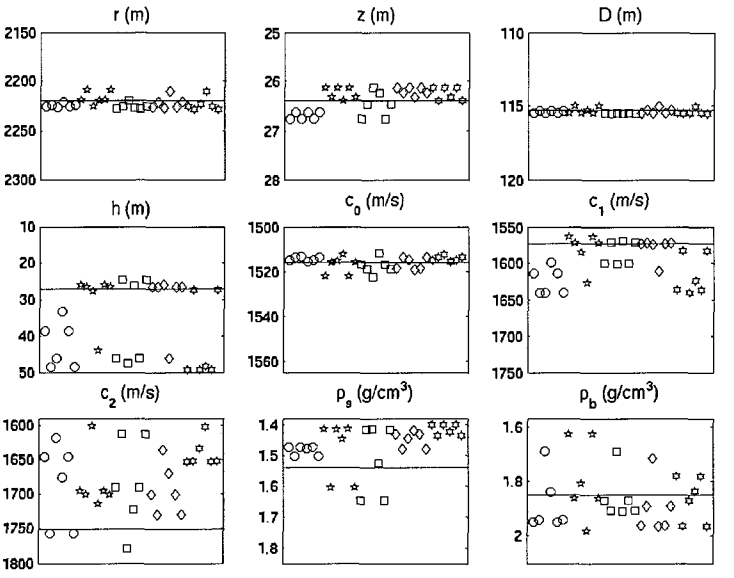

Figure 4.8: GA inversion results for noisy synthetic data. Each symbol represents a different noise realization (six independent inversions per noise realization). Solid lines represent the true parameter values.

for these data this model parameterization is suitable. The six unknown geoacoustic properties included in the inversion were the water depth, D, the sediment thickness, h, the sediment and basement sound speeds, c_s and c_b, and the density and attenuation of the entire seabed, ρ and α. Also included in the inversions were small corrections to the range and the source and receiver depths, but as these are nuisance parameters they are not discussed here.

Two MAPEX 2000 data sets are considered in this study. One was taken from the northern end of the track which was known to include a low-speed sediment layer. The other was taken from the southern end characterized by a more consolidated, higher-speed sediment (referred to as the low-speed and high-speed cases, respectively). Ten

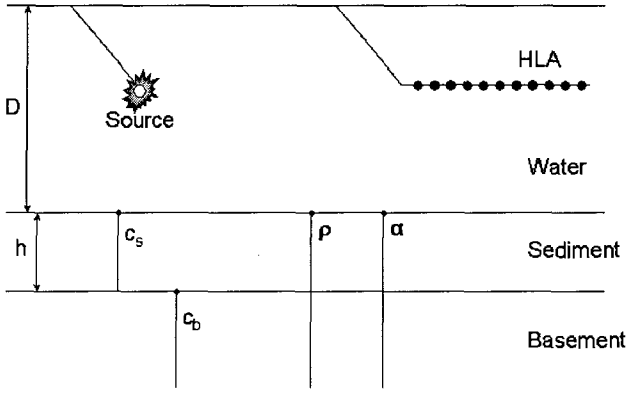

Figure 4.9: Schematic diagram of the ocean environment used for the inversions of the MAPEX 2000 data.

independent inversions were carried out for each data set. The objective function that was minimized was again based on the normalized Bartlett processor, except that it was summed coherently in frequency and incoherently over range.

Figure 4.10 shows the results of the ten independent inversions for the low-speed case. These results show considerable variability for the water depth, sediment thickness and sediment sound speed. This is likely due to the difficulty in determining these parameters for a low-speed sediment layer which appears acoustically similar to the water column, leading to strong correlations between D, h and c_s (Fallat et al., 2000, 2004). In general, the results obtained using ASSA show less variability for all parameters, and in particular for D, h, and c_s, than the results obtained using GA.

Figure 4.11 shows the inversion results for the high-speed case. These results show much less variability for D, h, and c_s than for the low-speed case (Fig. 4.10). The results obtained using ASSA show less overall variability than those using GA,

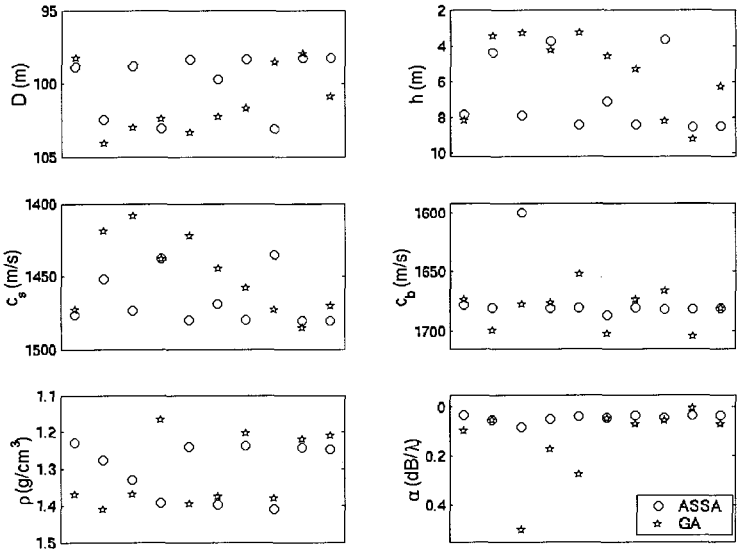

Figure 4.10: The results of ten independent inversions for the low-speed MAPEX 2000 site. The circles represent the ASSA results while the stars represent the GA results.

with the exception of the basement sound speed, where the results for both algorithms vary over roughly the same scale.

The objective function values obtained in all inversions are shown in Fig. 4.12. ASSA obtained the lowest objective function value for all of the 20 inversions carried out for the low-speed and high-speed cases.

Table 4.2 summarizes the mean parameter value and the average absolute variability for the ten inversions of each case for both ASSA and GA. The average variability for ASSA is lower than that for GA for all parameters in both cases. Note also that the mean parameter estimates for both inversion approaches are consistent within the average variabilities. The level of algorithm-induced variability for the

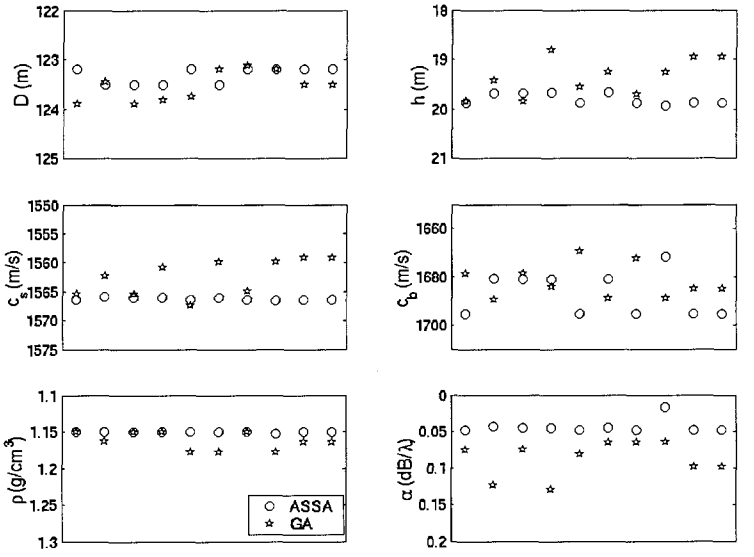

Figure 4.11: The results of ten independent inversions for the high-speed MAPEX 2000 site. The circles represent the ASSA results while the stars represent the GA results.

high-speed case would likely be considered negligible compared to other factors that influence the inversion results (e.g., measurement and theory errors, temporal and/or spatial variability in sound-speed profile). However, this is not necessarily true for the low-speed case.

4.4 Summary

Geoacoustic inversion techniques are frequently utilized for estimating seabed properties from measured acoustic data. Algorithm-induced variability represents an important issue in interpreting such inversion results in terms of spatial and/or temporal

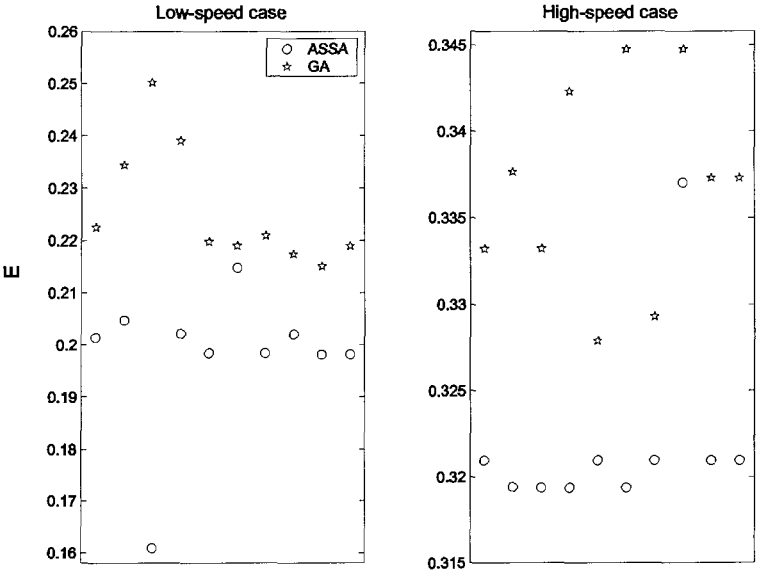

Figure 4.12: Objective function values for the inversions of MAPEX 2000 data.

variation of the environment. The intent of this chapter was to evaluate the variability of results for FSA, ASSA, and GA and to determine which algorithm preformed the best for this application.

In any comparison between algorithms it is important to ensure that an equal amount of care and attention is applied in running each algorithm. This has been addressed, in part, by considering a variety of control parameter settings for all three algorithms. It was found that the conclusions of the study were not strongly dependent on these control parameter settings. Also, I consulted at length with Peter Gerstoft, the author of the GA package SAGA, to ensure that it was run properly. Finally, all the inversions were run such that a similar number of forward models were evaluated.

ASSA generally produced the lowest objective function values and the lowest variability in the inversion results for all cases, followed by GA, with FSA producing results that were considerably poorer. The variability differed considerably between

Table 4.2: Mean and average absolute variability (AV) of the inversion results for the MAPEX 2000 data.

	Low-speed case				High-speed case			
Properties	ASSA		GA		ASSA		GA	
	Mean	AV	Mean	AV	Mean	AV	Mean	AV
D (m)	100.1	1.7	101.2	1.8	123.3	0.1	123.5	0.2
h (m)	6.9	1.7	5.6	1.9	19.8	0.1	19.4	0.3
c_s (m/s)	1466.2	14.6	1449.3	22.6	1566.3	0.2	1562.5	2.8
c_b (m/s)	1679.4	3.8	1680.9	12.8	1687.2	8.1	1685.0	8.5
ρ (g/cm^3)	1.29	0.06	1.31	0.08	1.15	0.0005	1.16	0.01
α (dB/λ)	0.04	0.008	0.14	0.1	0.07	0.005	0.08	0.02

noise-free synthetic data, noisy synthetic data, and the low- and high-speed measured-data cases. This indicates that the variability should be evaluated on a case-by-case basis. For example, the algorithm-induced variability for the high-speed case was likely negligible compared to other uncertainties. However, significant variability was found for the low-speed case. In fact, the variability for this case was comparable to that which has been interpreted as due to temporal and spatial variability in previous studies (Siderius et al., 2001; Snellen et al., 2001; Siderius et al., 2002; Fallat et al., 2004). The variability in the results was exacerbated by inter-parameter correlations, which sometimes resulted in convergence to local minima.

Finally, it should be emphasized that the variability inherent in inversion results (considered here) does not quantify the uncertainty of parameter estimates, which must also include consideration of the effects of data and theory errors mapped to variability in model parameters (Dosso, 2002; Dosso & Nielsen, 2002).

Chapter 5

ASSA Inversion of Synthetic and Experimental Data

This chapter describes the results of ASSA inversions of synthetic and experimental data. The previous chapter showed that ASSA induced the least amount of variability and produced inversion results with the lowest objective function values therefore it is applied here. The synthetic acoustic data were generated using the range-dependent propagation model RAMGEO (Collins, 1993). The measured acoustic data were taken from the MAPEX 2000 and BOUNDARY 2003 experiments. Portions of this chapter have appeared in a journal article and two conference proceedings (Fallat, Nielsen, & Dosso, 2004; Fallat, Nielsen, Dosso, & Siderius, 2005a; Fallat et al., 2005b).

5.1 Synthetic Data Inversions

Synthetic data are considered here first to examine issues of sediment layer resolution and parameter sensitivity in a controlled study where the true model is exactly known. The synthetic data were generated using an environment that consisted of

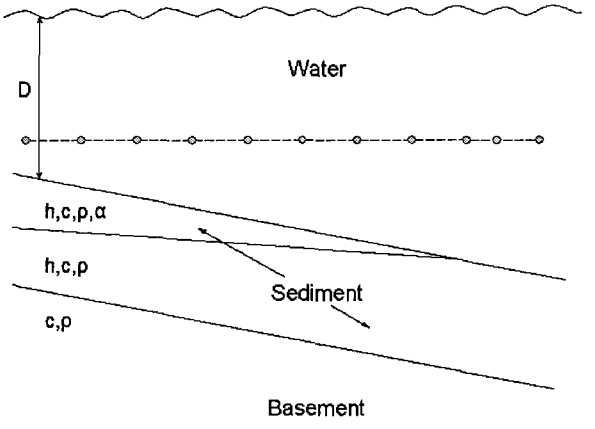

Figure 5.1: Diagram of the synthetic environment. The circles represent the locations where inversions were carried out.

both range-dependent bathymetry and geoacoustic properties as shown in Fig. 5.1. The environment was designed to simulate the characteristics of the work area, in particular the information from the seismic profile and core samples (see Chapter 3). To that end, the environment consisted of two sediment layers over a basement. The top sediment layer became thinner with range until it disappeared completely. The second sediment layer had a constant separation of 20 m from the water-sediment interface. In each of the sediment layers and in the basement, the geoacoustic properties were assumed to be constant both in range and depth.

The synthetic data were generated using the range-dependent propagation model RAMGEO (Collins, 1993). Gaussian noise was added to the data to achieve a signal to noise ratio of 10 dB. Since the two experiments were conducted along essentially the same track the only differences in the synthetic data were the frequencies and the receiver arrays. For the MAPEX 2000 scenario the data covered the frequency band

250–750 Hz in 50 Hz increments recorded at a 252 m array. For the BOUNDARY 2003 scenario the data covered 850–1850 Hz in 50 Hz increments recorded at a 35 m array.

An important aspect for practical geoacoustic inversion is determining a suitable environmental parameterization given the resolving power of the data. The primary issue involves choosing the number of seabed layers to include; too few layers will not properly represent the environment, while too many layers can introduce erroneous structure that is not warranted by the data. One approach is to carry out several inversions starting from a simple model and successively adding layers to determine a parameterization where the addition of a layer does not significantly decrease the objective function (Fallat, 1999; Dosso et al., 2001). The parameterization is a particularly interesting issue here, since the seismic profile (Fig. 3.15) and the corresponding simulated environment (Fig. 5.1) both involve a three-layer environment transitioning to a two-layer environment. To address this, two environmental parameterizations are considered for the inversions. The first parameterization consists of a single sediment layer over a semi-infinite basement layer, while the second consists of two sediment layers over the basement (referred to as the two- and three-layer cases respectively).

A secondary issue in parameterization is determining which geoacoustic parameters to include for each layer. Previous studies have shown that some parameters are relatively insensitive and are poorly determined in inversion (Fallat et al., 2000, 2004; Siderius et al., 2002). Including insensitive parameters generally increases the computational effort of the inversion without providing more meaningful results. In such cases, it may be preferable to hold insensitive parameters at physically meaningful values. For the synthetic data inversion, each layer was characterized by its thickness, h, sound speed, c, and density, ρ. Attenuation (α) was included only in the upper sediment layer, as attenuation is well known to be insensitive in short-range inversions (the attenuation of the deeper layers was held fixed at their true values,

Table 5.1: Summary of the geoacoustic properties used to generated the synthetic data.

Geoacoustic property	Sediment (1^{st} layer)	Sediment (2^{nd} layer)	Basement
c (m/s)	1480	1550	1685
ρ (g/cm^3)	1.4	1.65	1.8
α (dB/λ)	0.1	0.15	0.2

Table 5.1). The water depth, D, was also included in the inversions as this is typically a sensitive parameter. The values used to generate the synthetic data are given in Table 5.1. Relatively conservative search bounds were used for all the parameters as given in Table 5.2. The water depth was bounded to be within 2.5 m of the true value since this property is generally known approximately from echosounder measurements. The sound speed in the second layer was constrained to be larger than in the first layer. Finally, small corrections to the nuisance parameters range and source/array depths were included in the inversions.

Figure 5.2 shows the inversions results for the MAPEX 2000 scenario for the two- and three-layer parameterizations. For the two-layer case the results for the water depth (top panel) are in good agreement with the true values for the first three points after which the water depth closely approximates the bottom of the first sediment layer until it disappears. The inversion results for the sediment depth (top panel) show significant variability out to a range of 5 km. Beyond 5 km the inversion results are in very good agreement with the true value of the second layer. Note that sediment depth refers to the depth from the sea surface while sediment thickness refers to the depth from the water-sediment interface.

The sound speeds (middle panel) of the sediment and basement layers are reasonably well-determined with the exception of the basement speed for the first few points. From 0–5 km the sediment speed closely approximates the true speed of the

Table 5.2: Summary of the search bounds used for the inversions. The superscripts 1 and 2 denote the first and second sediment layers and the subscripts s and b represent the sediment and basement speeds.

Two-layer parameterization			**Three-layer parameterization**		
Geoacoustic property	Lower bound	Upper bound	Geoacoustic property	Lower bound	Upper bound
D (m)	true–2.5	true+2.5	D (m)	true–2.5	true+2.5
h (m)	1	30	h^1 (m)	1	15
–	–	–	h^2 (m)	1	30
c_s (m/s)	1460	1650	c_s^1 (m/s)	1460	1650
–	–	–	c_s^2 (m/s)	1460	1850
c_b (m/s)	1550	1900	c_b (m/s)	1550	1900
ρ (g/cm^3)	1.2	2.15	ρ (g/cm^3)	1.2	2.15
α (dB/λ)	0	1.0	α (dB/λ)	0	1.0

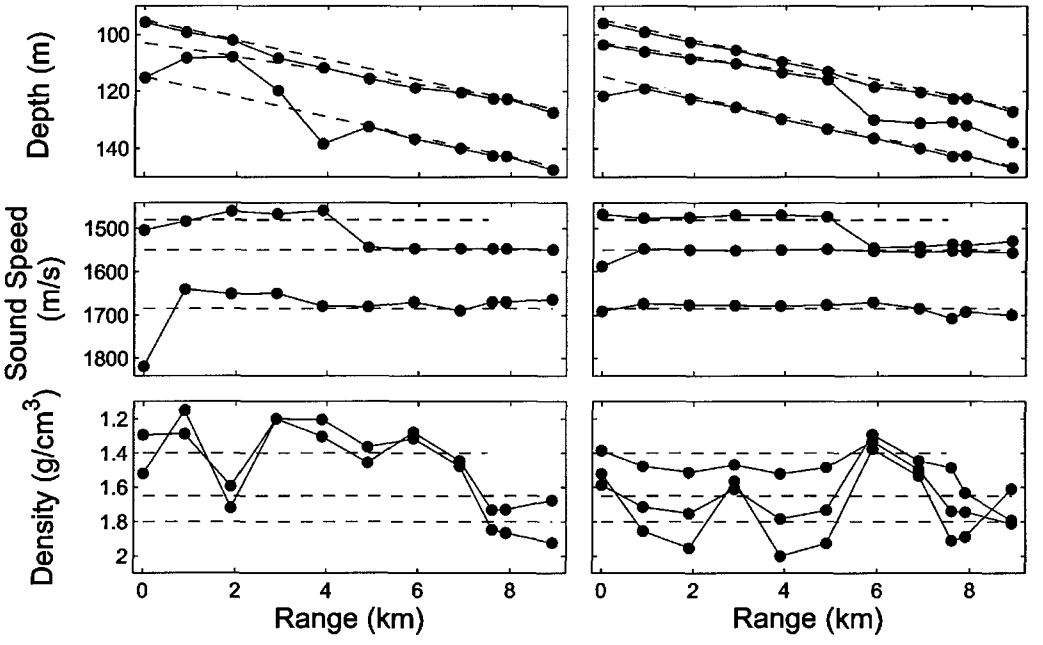

Figure 5.2: ASSA inversion results for the synthetic MAPEX 2000 data, showing the two- (left) and three-layer (right) cases. The true values are denoted by the dashed lines.

top layer. Beyond 5 km the sediment speed begins to follow the speed of the second layer. The basement speed is in good agreement with the true values with the exception of the first few points. The density (bottom panel) is poorly determined for almost all points. The results for the attenuation in the top layer are poorly determined with values distributed randomly over the search interval and therefore are not shown here.

The results for the three-layer case show considerably less variability than those for the two-layer case for the depths and sound speeds. The water depth closely follows the true value for almost all points. The results for the depth of the first sediment layer agree with the true value out to 5-km range. Beyond that, the results approximate the middle of the thicker sediment layer. The results for the second sediment layer closely follow the true value for all points except the first. The inversion results for sound speed of the first layer agree well with the true value for the upper layer out to 5 km; beyond this the results approximate the speed of the second layer. The inversion results for the speed in the second sediment layer and the basement agree well with the true values at all ranges (except the first point). Note that beyond 5 km the two sediment layers have essentially no sound-speed contrast and appear acoustically as one layer. As in the two-layer case, the results for density are generally in poor agreement with the true values.

The inversion results for the synthetic BOUNDARY 2003 data are shown in Fig. 5.3. For the two-layer case, the water depth is in good agreement with the true value. The results for the sediment depth show greater variation compared to the MAPEX 2000 scenario. That being said, taken together, the layer-thickness and sound-speed results seem to make sense. The results out to 4 km are generally poor but beyond that it appears that the inversions obtain a sediment thickness and sound speed that approximate the average of the two layers. The results for the basement sound speed are overestimated for all points and show substantial variation which

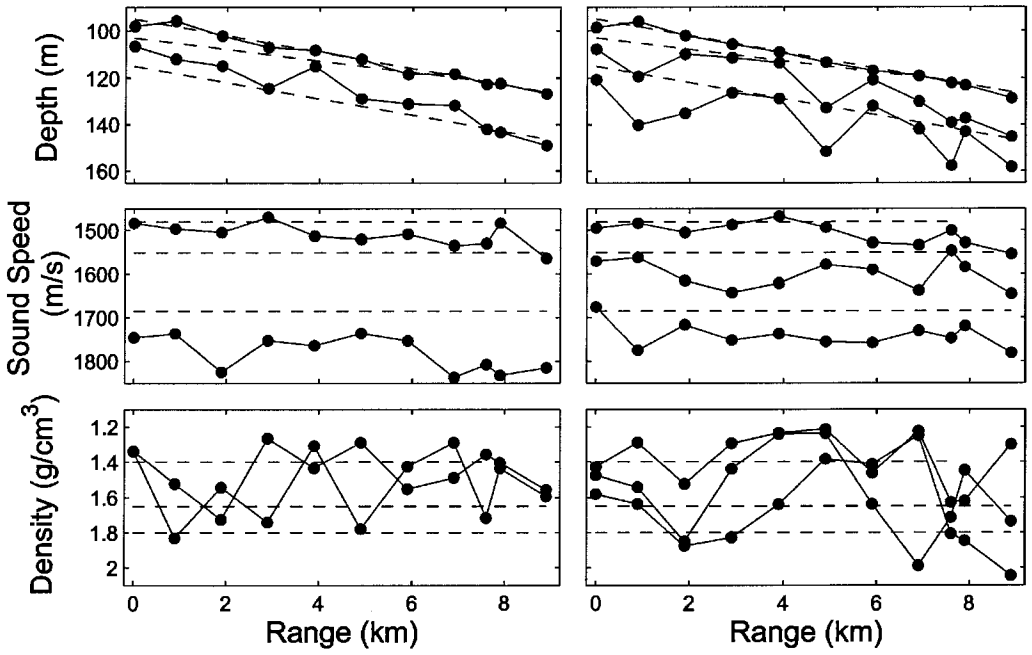

Figure 5.3: ASSA inversion results for the synthetic BOUNDARY 2003 data, showing the two- (left) and three-layer (right) cases. The true values are denoted by the dashed lines.

likely results from the limited penetration depth of the higher-frequency acoustic energy. The inversion results for the density are poor.

The inversion results for the three-layer case show, in general, that none of the boundaries or sound speeds are properly matched in a consistent way, with the exception of the water/sediment interface and the sediment sound speed in the first layer. These results demonstrate that for this experimental set up (i.e., higher frequency and shorter array) the inversions are only able to accurately resolve the upper-most geoacoustic properties.

The mismatch values obtained in the inversions are shown in Fig. 5.4. For reference, a mismatch value of approximately 0.1 was obtained for the true parameters

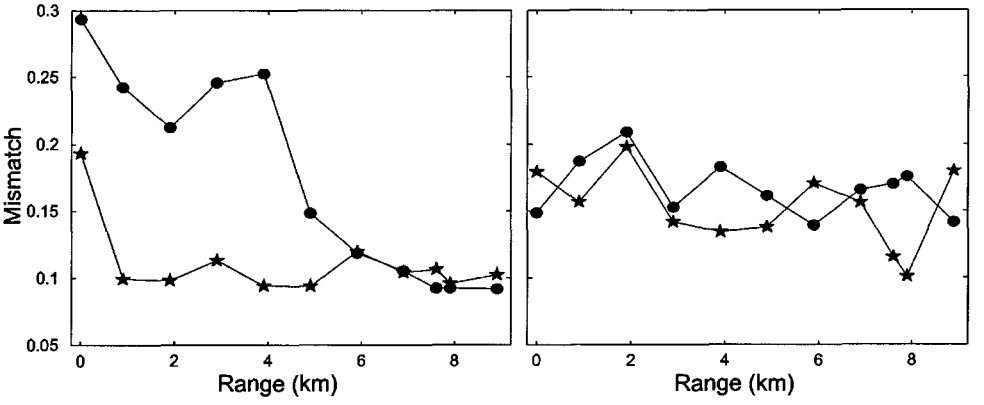

Figure 5.4: Mismatch values for the synthetic MAPEX 2000 (left) and BOUNDARY 2003 (right) data, showing both the two- (circles) and three-layer (stars) cases.

representing the mismatch between the models for noisy data. For the MAPEX 2000 scenario the mismatch values for the two-layer case do not match the data as well as the three-layer case out to a range of 5 km. From 6 km and beyond the two cases produced essentially the same mismatch. This means that out to 5-km range three layers can be resolved while beyond 5 km including a third layer does not significantly reduce the mismatch, and hence only two layers are resolved. In the BOUNDARY 2003 scenario there is no significant difference between the two- and three-layer parameterizations, which means that a more complicated three-layer model is not warranted for this scenario.

The above results suggest that for the MAPEX 2000 scenario the inversions are able to resolve three layers when these layers influence the acoustic propagation. Once the top sediment layer became too thin the two- and three-layer parameterizations matched the data to essentially the same level. This is also seen in the inversion results, for the two-layer case the results did not closely approximate the true values until beyond 6 km, while the results for the three-layer parameterization closely approximated the true values for the entire track. For the BOUNDARY 2003 scenario

the inversion results were not as stable as for the MAPEX 2000 scenario. In particular, only the upper-most geoacoustic properties were resolvable. Also, the three-layer environment was poorly resolved over the entire track.

5.2 Experimental Data Inversions

5.2.1 MAPEX 2000 Inversions

In this section, the MAPEX 2000 experimental data are inverted. The same inversion technique, parameterizations, and search bounds (Table 5.2) used in the previous section are also applied here. The exception is that the seabed density is represented by a single (depth-independent) value since the data were insensitive to this parameter.

Figure 5.5 shows the inversion results for the two-layer parameterization. Inversions were carried out at 37 locations along the experiment track (see Fig. 3.2). The results for the water depth and the sediment depth are superimposed onto the high-resolution seismic profile. Note that the seismic and experimental tracks were not exactly aligned (see Fig. 3.2) and therefore a perfect agreement may not be possible. The inversion results for the water depth are in good agreement with the water-sediment interface out to a range of 6 km. Beyond 6 km the top sediment layer is too thin to resolve, and the results of the water depth vary between the water-sediment interface and the bottom of the inclusion. The average difference between the inversion results and the measured bathymetry was < 1 m. The results for the sediment depth are quite stable (i.e., there is little variation between subsequent points) and closely follow the bottom of the inclusion out to around 2 km. At 2 km there is a significant change and the sediment depth starts to follow the boundary of the basement for the rest of the track except for two outliers between 6–8 km. The outliers at ~ 6.5 and 7 km appear to be instances when the sediment depth again approximates the bottom

of the inclusion. It is interesting to note that at these points the results for the water depth also agree with the depth of the water-sediment interface. The general sloping trend of the bottom of the inclusion and the boundary of the basement is matched quite well by the inversion results.

The inversion results for the sediment (topmost results) and basement sound speeds are shown in the middle panel of Fig. 5.5. The sediment sound speed values generally appear correlated with the sediment depth, i.e., the sound speed increases (decreases) when the depth increases (decreases). For ranges from 0–2 km the sediment sound speeds are relatively low, with an average value of 1480 m/s. This is in general agreement with northern core measurements, which indicate a sound speed of approximately 1460 m/s over the top 1.2 m, particularly since the sound speed likely increases below the maximum core depth and the inversion results average over the sediment layer ($\sim$ 8 m). For ranges beyond 7 km (where the low-speed inclusion is negligible), the average sound speed of the inversion results is 1562 m/s. This is also in general agreement with the properties observed in the southern cores, which indicate a sound speed that increases from an initial low value to approximately 1550 m/s at 0.5 m depth. From 2–6 km range, the inversion results have an average sound speed of 1535 m/s, which is consistent with averaging over the two sediment layers, as indicated by the seismic profile.

Unfortunately, the core data do not extend deep enough into the sediment for comparison with the basement sound speed obtained by the inversions. However, the variation in inversion results provides an indication of the stability of the estimates. Since this deeper layer is expected to be range-independent over this scale ($\sim$ 10 km), the inversion results should show little variation. In the region from 0-4 km there is more variation in the results compared to the rest of the track. This is likely due to the fact that in this region there are three layers yet the inversion is restricted to two layers. Therefore, the speeds in the layers are being depth-averaged. In the region

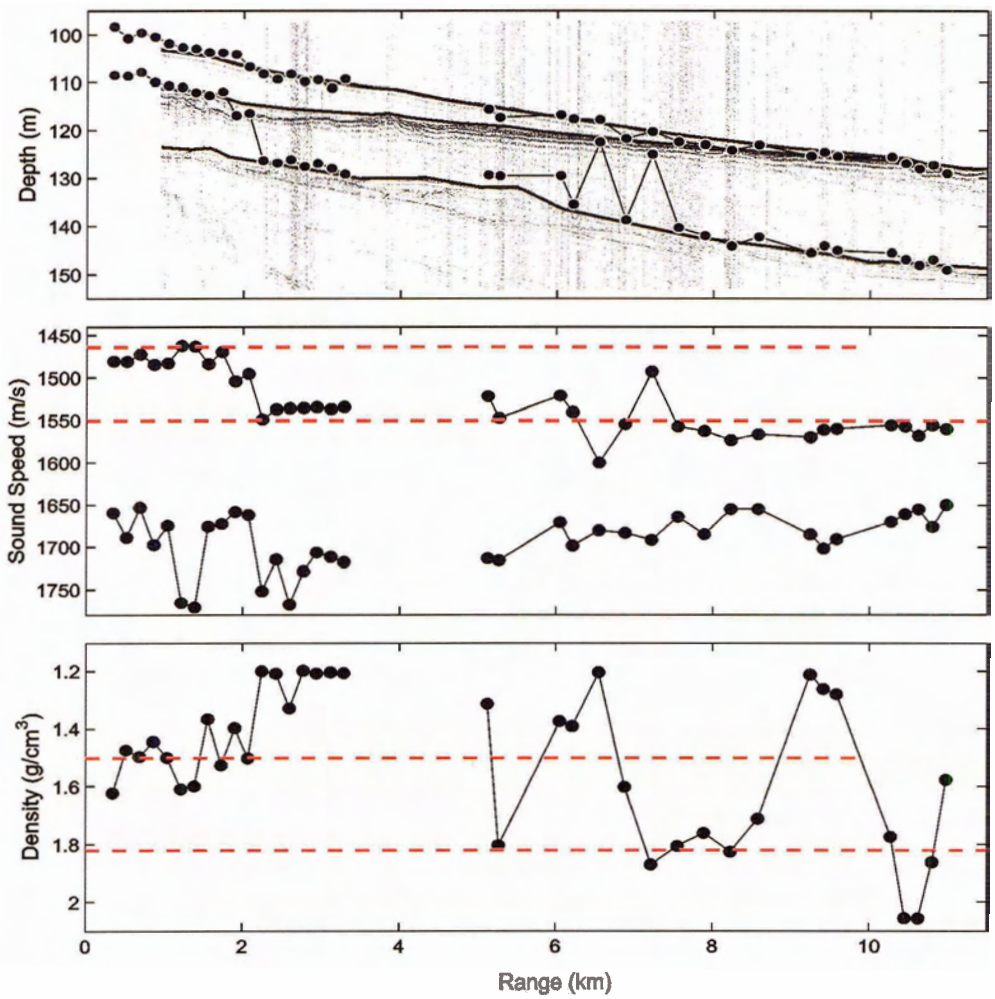

Figure 5.5: Inversion results for the MAPEX 2000 data for the two-layer parameterization. The solid lines are interpretations of the significant reflectors. The red dashed lines are estimates from the core samples.

between 5-10 km the results are quite stable with a maximum variation of 50 m/s.

The inversion results for density (bottom panel of Fig. 5.5) are quite variable. However, the results for ranges 0–2 km (where the low-speed inclusion is thickest) show less variability and have an average of 1.39 g/cm^3 which somewhat agrees with the density estimate from the northern core. The results beyond 5 km have an average value of 1.62 g/cm^3. Although these results include large fluctuations, the trend of increasing density with moving from north to south is seen here as well as in the cores.

The inversion results for the three-layer case are shown in Fig. 5.6. The upper panel shows that the water depth is in good agreement with the water-sediment interface out to 6-km range. Beyond this range the low-speed inclusion is very thin and the water depth varies between the water-sediment interface and the bottom of the inclusion as they merge. The inversion results for the depth of the first layer follow the second reflector over 0–2 km range where the inclusion is thickest. Beyond 2 km, the inclusion appears to be too thin to be resolved acoustically, and the depth follows the third reflector (with a few exceptions where they match the second reflector). The acoustic basement is the most poorly determined interface. A number of the inversion results out to 3-km range approximately agree with the third reflector. Some of these results may also intermittently agree with a possible deeper reflector (dashed line). Beyond 6-km range the inversion results for the basement interface are fairly consistent at 160-170 m and suggest a downward slope to the south, in agreement with the reflectors above. It is possible that these results delineate a deeper reflector, below the maximum depth of the seismic data, or they may simply accommodate the third layer required by the parameterization. From the above, it appears that the three-layer inversion can approximately resolve the three-layer structure seen in the seismic profile for a number of points out to 2 km range. Beyond 2-km range the inclusion is generally not resolved, and the inversion results may or may not be

sensitive to deeper reflectors.

The results for sound speed are shown in the middle panel of Fig. 5.6. The results for the first sediment layer are similar to those for the two-layer case, with average sound speeds of 1484 m/s from 0–2 km, 1529 m/s from 2–6 km and 1560 m/s beyond 6 km. These values are again in agreement with the core measurements. The sound speeds of the deeper layers show greater variability, indicating that they are not well determined. Average values for the second sediment layer (dashed line) and the basement are 1648 m/s and 1700 m/s, respectively. The results for density (bottom panel), indicate a lower density out to 2 km range (average of 1.31 g/cm^3) than beyond 6 km (average of 1.54 g/cm^3), but exhibit large fluctuations, indicating poor resolution.

The mismatch values obtained by both the two- and three-layer cases are shown in Fig. 5.7. Out to 3-km range the mismatches are usually slightly smaller for the three-layer case than for the two-layer case, but the differences are very small. Beyond 3 km neither case provided consistently lower mismatches. This indicates that including three layers in the inversion did not significantly improve the ability to fit the measured acoustic fields, and that three layers are not well resolved (particularly beyond 3 km).

5.2.2 BOUNDARY 2003 Inversions

In this section the inversion results for the BOUNDARY 2003 experiment data are described. Since the inversion of the synthetic data showed that for this scenario the three-layer model was poorly resolved only a two-layer parameterization was used.

For the BOUNDARY 2003 data, 41 independent inversions were carried out and the results are shown in Fig. 5.8. The results for the water depth are in good agreement with the water-sediment interface. The results are more variable than for the

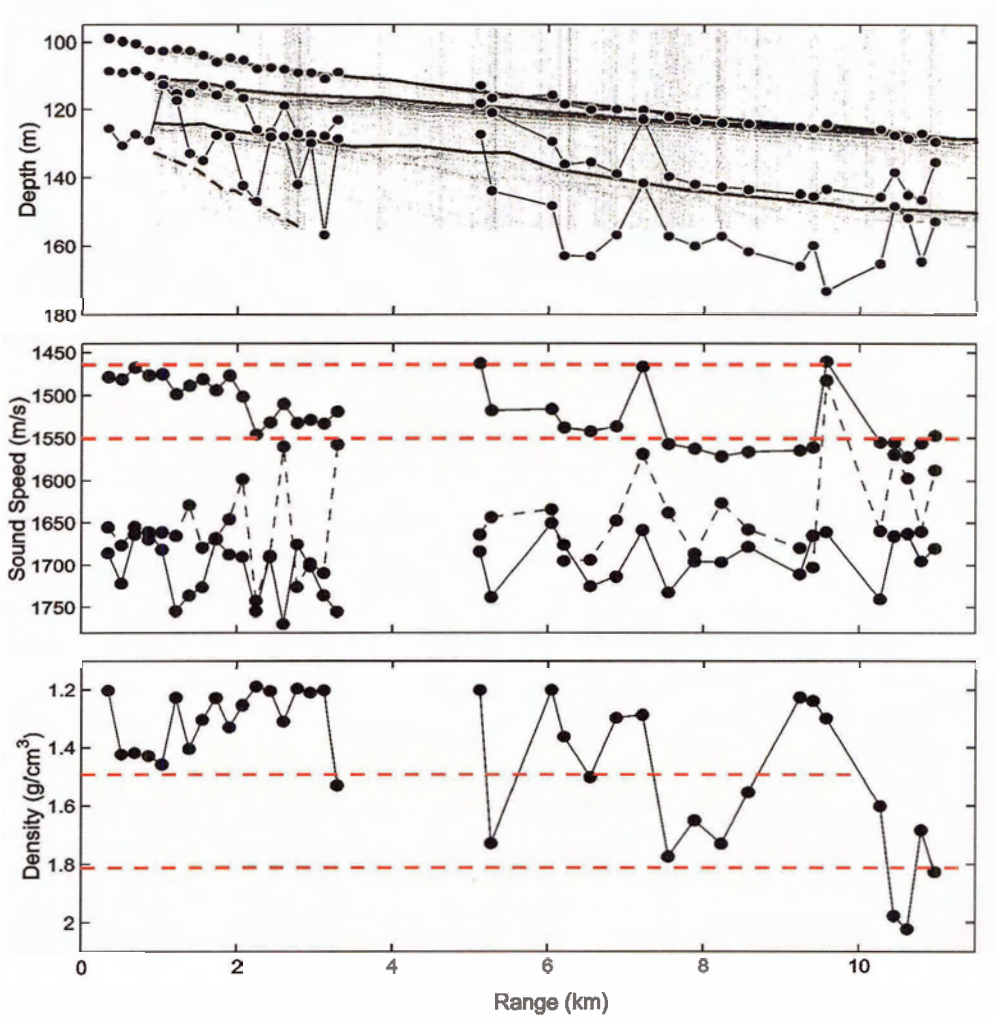

Figure 5.6: Inversion results for the MAPEX 2000 data for the three-layer parameterization. The black dashed line in the middle panel represents the sound speed in the second sediment layer.

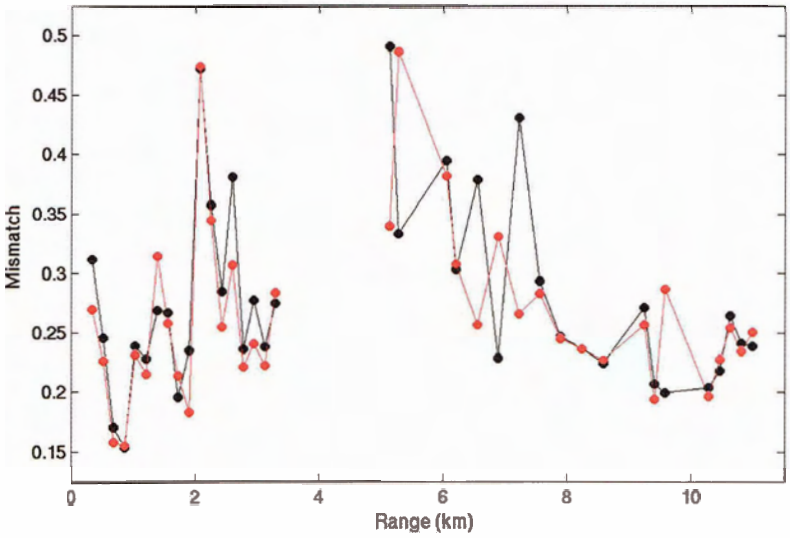

Figure 5.7: The final mismatches for the inversions of the MAPEX 2000 experimental data. Included are both the two- (black) and three-layer (red) parameterizations.

MAPEX 2000 data, in particular, they show more variation about the water-sediment interface. The results for the sediment depth are generally in poor agreement with the layering structure seen in the seismic profile. There are a few points along the track where the inversion results appear to be approximating the structure but there is considerable variability.

The inversion results for the sediment and basement sound speeds are shown in the middle panel. The results for the sediment sound speed from 1.5-3.5 km are in good agreement with the sound speed measured from the northern core sample. Between 3.5-6 km the sediment sound speed is quite high and does not agree with either of the speeds measured from the core samples. Finally, from 6 km to the end of the track the sediment sound speed, with the exception of three points, varies between the values measured from the core samples. The inversion results for the basement

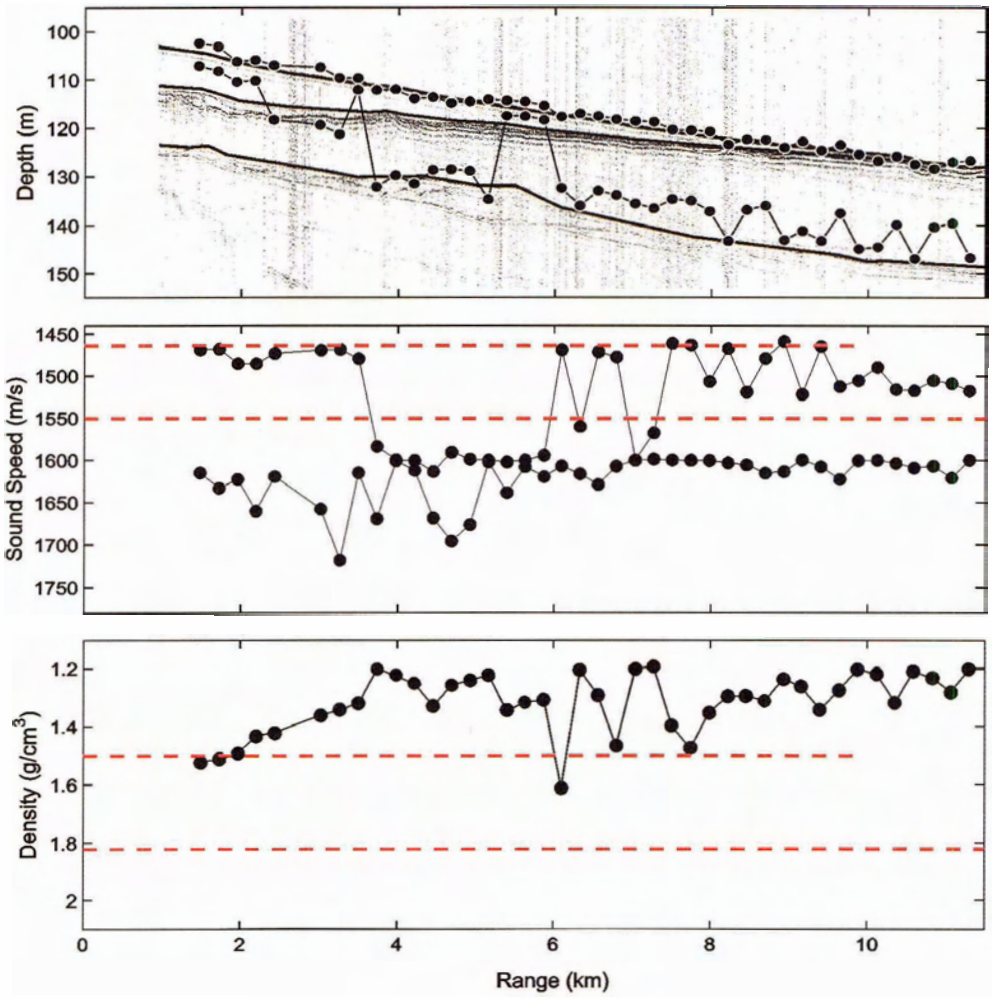

Figure 5.8: Inversion results for the BOUNDARY 2003 data for the two-layer parameterization.

sound speed show substantial variability between the start of the track and 5.5 km. Beyond 5.5 km the results are stable with variations of less than 50 m/s.

The results for density are shown in the bottom panel. These results are more stable than the MAPEX 2000 results but generally have a lower density than what was measured in either of the core samples.

The mismatches obtained by the inversions are shown in Fig. 5.9. The average value is 0.28 which is similar to the values obtained for the MAPEX 2000 inversion (see Fig. 5.7). It is interesting to note that the mismatches at the start (first eight) and end (last six) of the track are lower than the rest of the track. These mismatches correspond to locations where the results for the sediment sound speed are very stable (see middle panel of Fig. 5.8). It would appear that the data are sensitive to the uppermost sediment sound speed when the layer is thick enough (i.e., no averaging over deeper layers). This is the case for the first eight points where the low-speed inclusion is approximately 6-8 m thick and for the last six points where the inclusion has essentially disappeared.

5.2.3 Summary

The inversions of the experimental data show several interesting outcomes. First, the technique is capable of characterizing some features of the range-dependent environment using a series of short-range, range-independent inversions. The caveat to this is that special care must be taken when parameterizing the environment. In the MAPEX 2000 case, the data were only able to resolve a two-layer environment even though it was known *a priori* that for a portion of the track there were three layers. That begin said, the results for the two-layer environment closely matched the ground-truth information. For the BOUNDARY 2003 case even the two-layer environment was not determined very well.

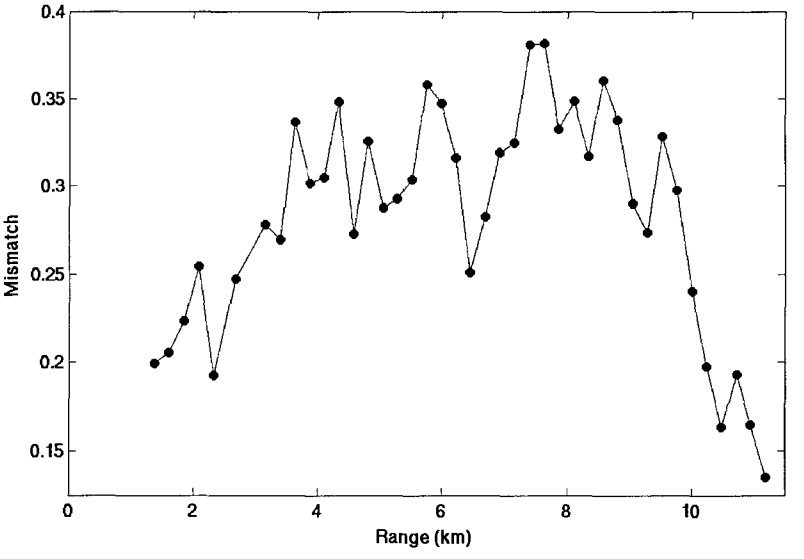

Figure 5.9: The final mismatches for the inversions of the BOUNDARY 2003 experimental data.

The second interesting outcome is that the MAPEX 2000 scenario produced results that were in better agreement with the environmental data (i.e., seismic and core data) and were more consistent from one inversion to another. This is likely due to two factors. First the array was considerably longer in the MAPEX 2000 case and therefore recorded acoustic energy that interacted with the bottom at a larger range of grazing angles. Second, the source used during BOUNDARY 2003 produced a swept signal that was at a higher frequency than during the MAPEX 2000 experiment. This means that for the BOUNDARY 2003 scenario knowledge of the theory errors is more important and that the acoustic energy will not penetrate as deep into the sediment therefore making it more difficult to determine accurately deeper properties.

Chapter 6

Bayesian Analysis

6.1 FGS Inversions

This chapter describes the Bayesian analysis of the MAPEX 2000 experimental data using a fast Gibbs sampling (FGS) approach. Some preliminary analysis has already appeared in a peer-reviewed conference proceeding (Fallat et al., 2005a). For the present work, 18 of the 37 data sets along the MAPEX 2000 track are analyzed, because it is expected that the uncertainty estimates will be locally representative and the FGS algorithm is computationally intensive. The motivation for this analysis is two-fold: first, to compare the results with the ground-truth information and second, to compare the FGS and ASSA inversion results, and thereby evaluate meaningful range dependence in the results. As stated in Sec. 2.2 the results obtained from the ASSA inversions are the maximum *a posteriori* or MAP model estimates and therefore for consistency they will be referred to as MAP estimates throughout this chapter.

The FGS analysis was carried out on a two-layer geoacoustic model since the analysis in Chapter 5 showed that the experimental data were unable to reliably resolve a three-layer model. The same unknown parameters are included here; i.e.,

water depth, sediment thickness, sediment and basement sound speeds, density in the sub-bottom and small corrections to the source/array range and depths. As in the previous chapters, the range and source/array depths are considered to be nuisance parameters in the inversion and are not discussed further. The prior distributions for all parameters were uniform with limits given in Table 5.2. Finally, the same frequency band (i.e., 250-750 Hz in 50 Hz increments) and array configuration (64 sensors spaced 4 m apart) are employed for this analysis.

As described in Chapter 2, the Bayesian analysis requires an estimate of the data variance which includes theory and measurement errors. Assuming independent, identically distributed Gaussian errors, Eqn. 2.29 provides an estimate of the variance based on the maximum-likelihood model (MAP estimate). The variance was computed here using the MAP model estimates obtained from the ASSA inversions in Chapter 5 and setting N_f equal to the number of frequencies (11). For the FGS analysis the convergence criterion (see Chapter 2) varied from 0.1-0.2 which resulted in, on average, 200,000 models being sampled. This required on average 7.5 hours on a 667-MHz Alpha workstation.

For FGS analysis it is often constructive to compute the ESNR (see Eqn. 2.31) for an impression of how the signal compares to all sources of error (measurement and theory). Figure 6.1 shows the ESNR values for the data sets analyzed here which represent an average ESNR value of 5.1 dB.

In this chapter most of the results are displayed as one- and two-dimensional (1-D and 2-D) marginal probability distributions which are represented by histograms of the sampled models. For 1-D marginal distributions, displayed on the same plot, the same bin size has been used and they have been normalized to unit area. The 2-D marginal distributions have the same number of bins for each parameter.

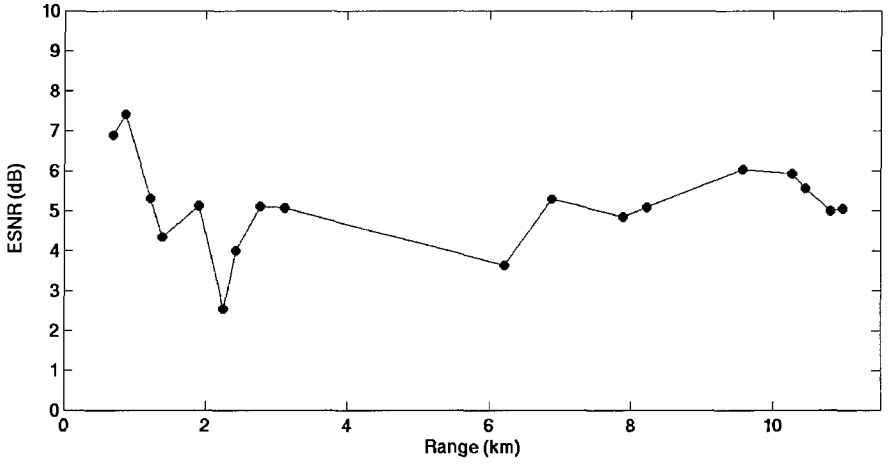

Figure 6.1: ESNR values for the MAP model estimates for the 18 data sets evaluated using FGS.

6.2 Marginal Probability Distributions

Figure 6.2 shows the 1-D marginal probability distributions for the water depth and sediment depth superimposed onto the seismic profile. In the region between 0-4 km the distributions for the water depth are quite broad. The reason for this is that this region is characterized by the low-speed inclusion which makes it difficult to determine accurately the water-sediment interface [see Chapters 4 and 5 and (Fallat et al., 2000, 2004)]. The low-speed inclusion is also the cause of the bi-modal marginal probability distributions seen between 6-8 km. At these ranges, where the sediment layer is thin but still significant, the samples alternate between the water-sediment interface and the bottom of the inclusion. For the remainder of the track, where the inclusion pinches out, the distributions for the water depth are narrow and well defined. It should be noted again that the seismic and experimental tracks were not exactly aligned (see Fig. 3.2) and therefore a perfect agreement is not expected. Figure 6.3 shows marginal distributions for the water depth for data sets at the northern and

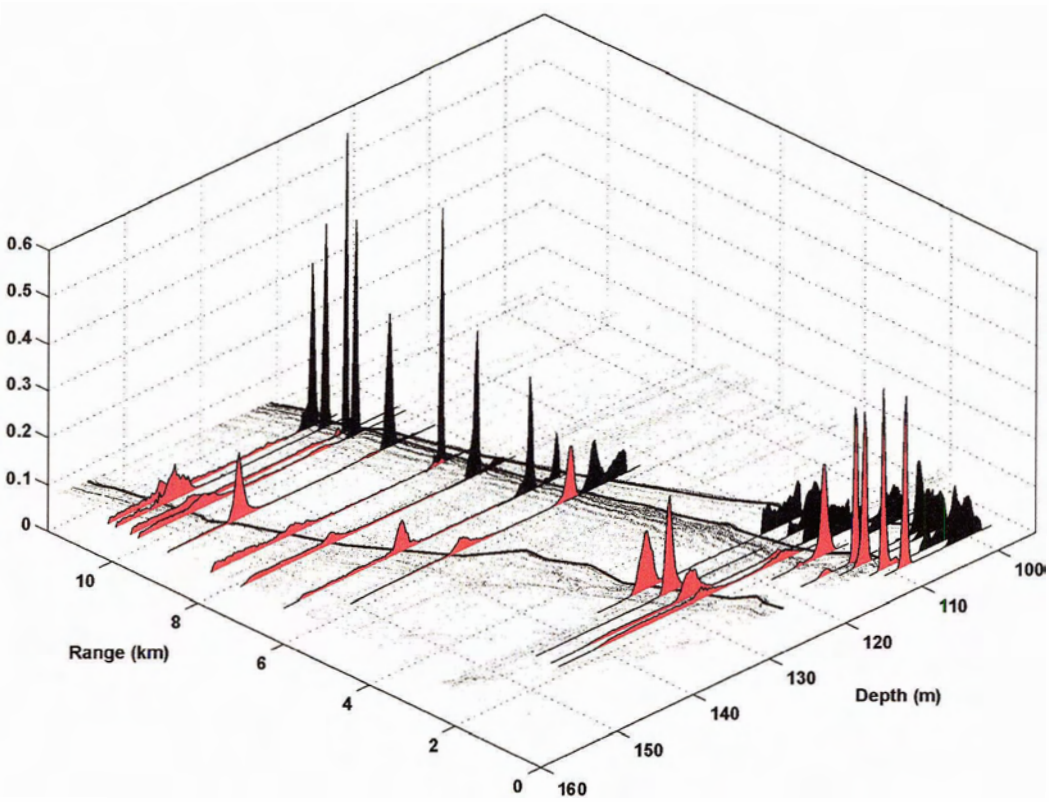

Figure 6.2: Marginal probability distributions for the water depth (black) and sediment depth (red) superimposed onto the seismic profile.

southern ends of the track. These marginal distributions illustrate the difference in the resolvability of the water depth between areas with low-speed (north) and high-speed (south) sediments.

The marginal distributions for the sediment depth (Fig. 6.2) follow the bottom of the inclusion out to approximately 2 km with well-defined, narrow distributions. Immediately beyond 2 km and at 6 km the marginal distributions are bi-modal, with one peak at the bottom of the inclusion and the other at the interface with the basement. At the other points along the track the marginal distributions for the sediment depth are either well defined at the interface of the basement or broad with

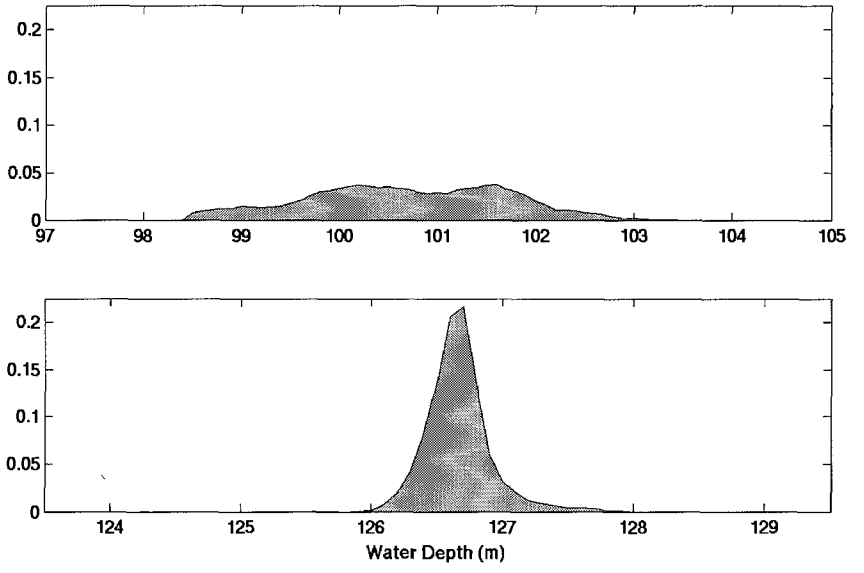

Figure 6.3: Marginal probability distributions for the water depth for the northern (top) and southern (bottom) ends of the track.

a slight peak located generally near the basement interface.

Figure 6.4 compares the marginal distributions and the MAP estimates for the sediment thickness (i.e., the depth from the water-sediment interface). In regions where the marginal distributions are broad the corresponding MAP estimates also show significant variation. For example, the marginal distributions near 8 km are essentially spread over much of interval. The MAP estimates close to this position alternate between thin and thick values. For this parameter, most of the MAP estimates (i.e., 12 of 18) are in good agreement with the main lobes of the marginal probability distributions. Importantly, the large-scale variations in the MAP estimates (e.g., the change in thickness at 2-km range) are also shown in the marginal distributions.

Figure 6.5 compares the marginal distributions for the sediment sound speed with

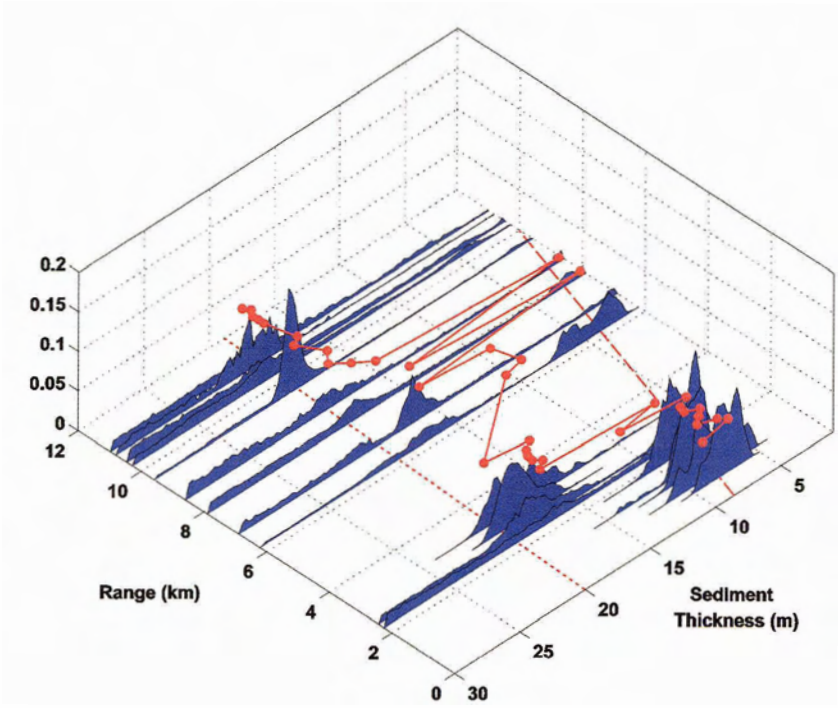

Figure 6.4: Marginal probability distributions and MAP estimates (red dots) for the sediment thickness. The dashed and dotted lines are layer depth estimates from the seismic profile. The MAP estimates have been plotted above the zero of the z-plane to improve the visibility.

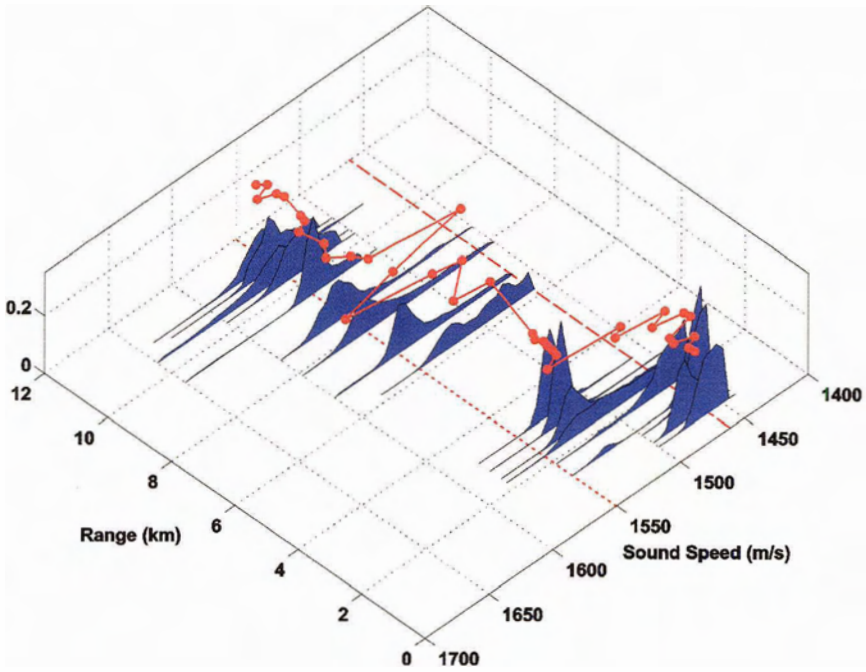

Figure 6.5: Marginal probability distributions and MAP estimates (red dots) for the sediment sound speed. The dashed and dotted lines are sound speed measurements from the northern and southern core samples respectively. The MAP estimates have been plotted above the zero of the z-plane to improve the visibility.

the MAP estimates. For most of the points the marginal distributions are reasonably well defined with widths of less than 50 m/s. In the region between 0-2 km range the main lobe of the marginal distributions are in good agreement with the low speed measured in the northern core samples. Between 2-4 km the marginal distributions provide a good approximation of a speed that has been depth-averaged over the two upper layers. For the ranges from 6.5-11 km the marginal distributions are in good agreement with the speed measurement from the southern cores. As with the sediment thickness most of the MAP estimates are in good agreement with the main lobes of the marginal distributions, including the large-scale variations.

The MAP estimates for the basement sound speed and marginal distributions for three different points along the track are shown in Fig. 6.6. A systematic increase in the basement speed with increasing range is shown in the marginal distributions. This is likely due to the depth-averaging of the speed in the upper two layers at short ranges where the low-speed inclusion is the thickest. For this comparison, the MAP estimates have been split into northern and southern groups with the separation occurring at 5-km range (where no inversions were carried out because of a course alteration, see Chapter 3). Overall, only four of the MAP estimates do not occur within the main lobes of the three marginal probability distributions. However, the northern group of MAP estimates show significant variation and are not consistent with the marginal distributions from the northern end of the track (0.7- and 3.1-km range). The southern group of MAP estimates shows less variation and are more consistent with the marginal distribution from the southern end of the track (9.6-km range).

Figure 6.7 shows 1-D marginal probability distributions for the density for data sets at the extremes of the experimental track. At the northern end of the track, where the inclusion is the thickest, the density is generally resolved to be between 1.1-1.8 g/cm^3. This is somewhat consistent with the density measurement from the northern cores but the uncertainty is high. At the southern end of the track the marginal probability distribution is broad, covering essentially the entire search interval.

6.3 Inter-parameter Correlations

Inter-parameter correlations result in an increase in the uncertainty of individual parameters and complicate the inversion by making it more difficult to resolve uniquely the correlated parameters. An effective method of investigating these correlations is to compute a correlation matrix (see Eqn. 2.12). In Fig. 6.8 the correlation matrix

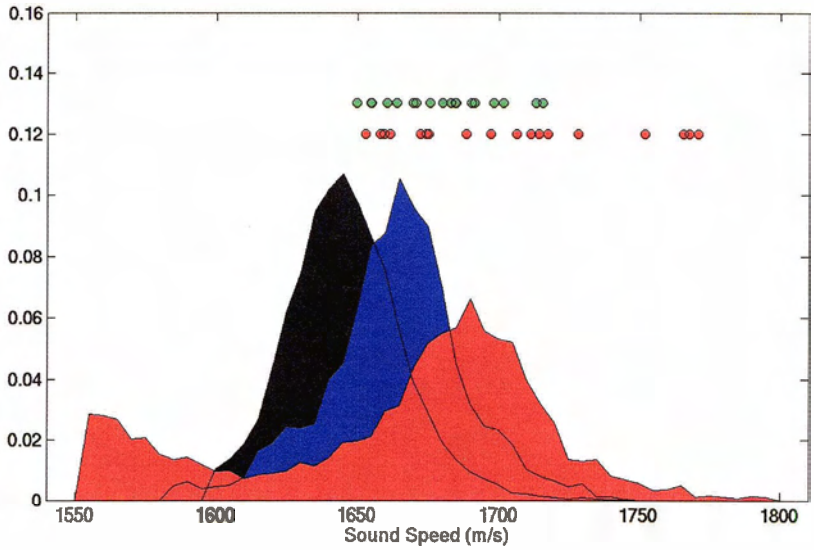

Figure 6.6: Marginal probability distributions for the basement sound speed from 0.7-km (black), 3.1-km (blue) and 9.6-km (red) range. The red and green circles represent the MAP estimates for the northern and southern ends of the track, respectively.

for water depth (D), sediment thickness (h) and sound speed (c_s), basement sound speed (c_b) and density (ρ) is shown for a data set at the northern end of the track. This figure illustrates a significant negative correlation between water depth and sediment thickness. This correlation results from the acoustic data's inability to resolve the boundary of the water column and the low-speed sediment layer which appears acoustically similar to the water (Fallat et al., 2000, 2004). There is also a somewhat weaker negative correlation between water depth and sediment sound speed. A positive correlation exists between the sediment thickness and sound speed which is likely a result of matching the data with parameter values that conserve the two-way travel time through the layer. Finally, it appears that there is a weak negative correlation between sediment sound speed and density. This correlation can be explained by

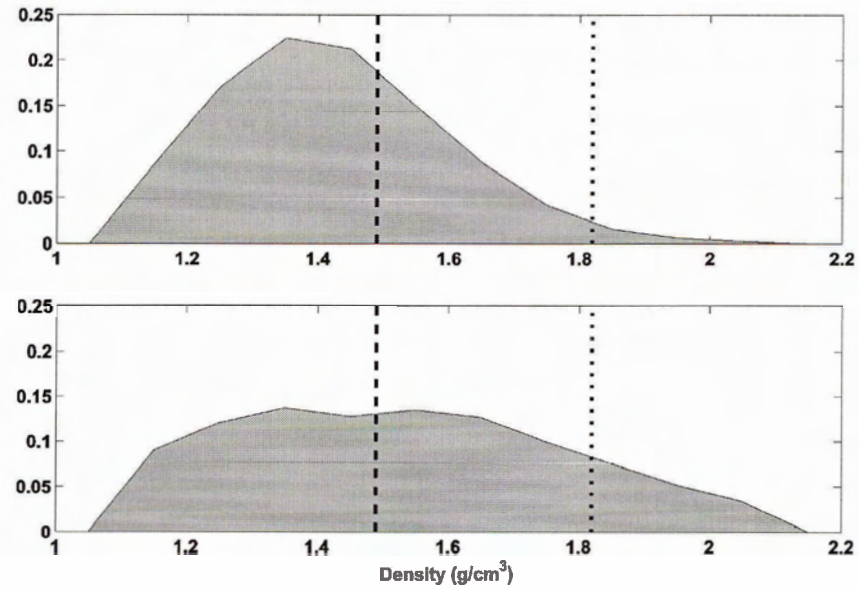

Figure 6.7: Marginal probability distributions for the density for northern (top) and southern (bottom) ends of the track. The dashed and dotted lines are density measurements from the northern and southern core samples respectively.

considering the reflection coefficient given by (Jensen et al., 1994):

$$R = \frac{(\rho_s c_s / \sin\theta_s) - (\rho_w c_w / \sin\theta_w)}{(\rho_s c_s / \sin\theta_s) + (\rho_w c_w / \sin\theta_w)}, \tag{6.1}$$

where the subscripts w and s denote the water column and sediment layer, respectively. Equation 6.1 shows that if the sound speed is increased and the density decreased the same value of R can be obtained, and vice versa.

It is interesting to further investigate the above correlations using 2-D (joint) marginal probability distributions. Figure 6.9 shows 2-D marginal distributions for combinations of the water depth, sediment thickness and sound speed for the same data set as in Fig. 6.8. Figure 6.9 (a) clearly illustrates the negative correlation between water depth and sediment thickness, i.e., high marginal probabilities are obtained for a range of parameter values provided the sediment thickness decreases as

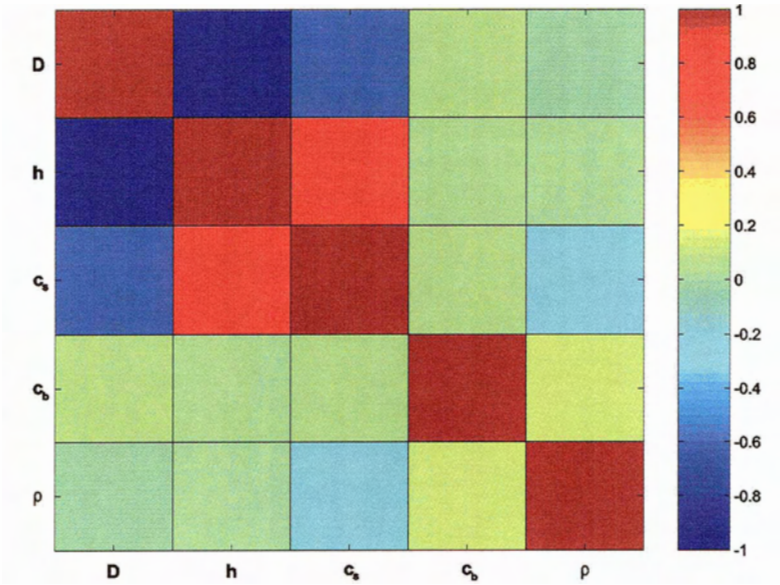

Figure 6.8: The correlation matrix for the geoacoustic parameters.

the water depth increases. In Fig. 6.9 (b) the positive correlation between sediment thickness and sound speed is plainly illustrated. Finally, the negative correlation between water depth and sediment sound speed is shown in Fig. 6.9 (c).

6.4 Summary and Discussion

In this chapter, the FGS algorithm was applied to the MAPEX 2000 experimental data to estimate the uncertainties associated with the geoacoustic properties. The objectives of this analysis were to compare the FGS results with the available ground-truth information and with the MAP estimates obtained by ASSA in Chapter 5.

The FGS results were generally in good agreement with the available ground-truth information. At the northern end of the track, where the low-speed inclusion is the thickest, the data were unable to resolve accurately the water-sediment interface. Once the low-speed inclusion became thinner this resolvability issue disappeared. For

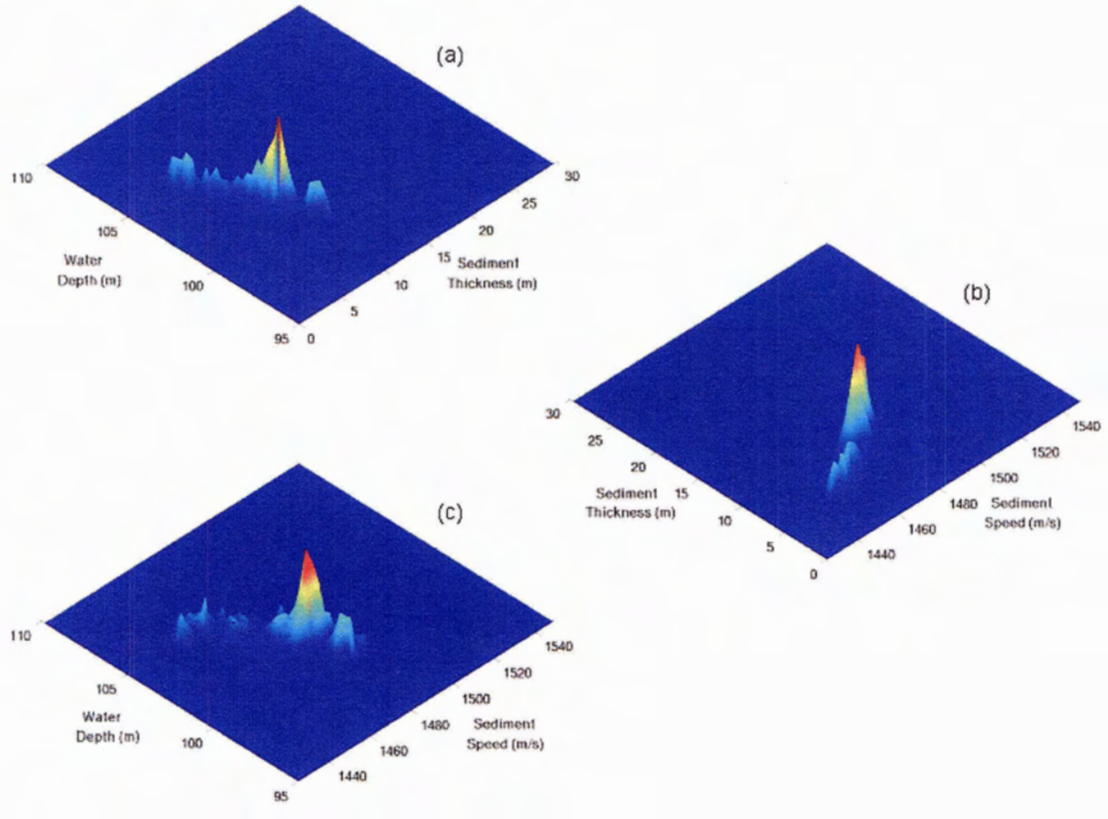

Figure 6.9: 2-D marginal probability distributions for the (a) water depth and sediment thickness, (b) sediment thickness and sound speed, and (c) water depth and sediment sound speed.

most of the track the data were able to accurately resolve a sediment depth that corresponded to the most significant acoustic interface. Out to a range of 2-km this interface was the bottom of the low-speed inclusion and for the ranges from 2-4 km and 7-10 km it was the interface of the basement. From 4-7 km, where the inclusion was pinching out, the data had difficultly resolving accurately the sediment depth.

The results for the sediment sound speed were in good agreement with the measurements from the core samples. In particular, they closely approximated the low-

speed and high-speed measurements and provided a reasonable estimate of a speed that was depth-averaged over the two upper layers. Unfortunately, there was no ground-truth information available for the basement sound speed. However, the results are generally consistent varying over 80 m/s. Finally, the data were unable to resolve accurately the density. At the start of the track there was possibly some agreement with the lower density value measured in the northern cores but there was high uncertainty in the results.

The second objective was to compare the results of the MAP estimates with the results from the FGS analysis. The goal of this comparison was to verify that the variability seen in the MAP estimates was from the range-dependence of the environment and not from other sources (i.e., idealized model parameterization, accuracy of forward model, error assumptions, etc). It should be noted that the ground-truth information provides a method of verifying whether the variability in the results is actually due to range-dependence in the environment. The caveat is that for this application ground-truth information will not always be available. Figures 6.4-6.6 showed that the majority of the MAP estimates were in good agreement with the main lobes of the marginal distributions. These figures demonstrate that the large-scale variation of the results (e.g., the pinching out of the low-speed inclusion and the increase in the upper sound speed from north to south along the track) is actually due to environmental range-dependence and not another source of variability. However, the smaller-scale variations (i.e., ping to ping fluctuations) appear to be the result of uncertainty/variability in the MAP estimates. This shows that the method developed here (i.e., combining the results of towed HA inversions) is capable of characterizing the dominant range-dependent features of the environment.

Chapter 7

Conclusions

Acoustic propagation in the underwater environment can be significantly influenced by interaction with the seafloor, particularly in shallow water areas. Therefore, to be able to predict accurately acoustic propagation in a shallow water environment knowledge of the properties of the seafloor is essential. In the past decade, considerable effort has been devoted to estimating these properties using geoacoustic inversion methods. In this thesis, a technique for characterizing a range-dependent environment by combining the results of a series of short-range, range-independent inversions was developed. This technique is one component of a "through-the-sensor" strategy that intends to make use of existing sonar systems to determine environmental properties.

The analysis consisted of two parts. First, the hybrid inversion algorithm adaptive simplex simulated annealing (ASSA) was employed to determine optimal estimates of geoacoustic properties at various points along an experimental track. Second, a Bayesian uncertainty analysis was carried out using fast Gibbs sampling (FGS). This uncertainty analysis is vital because it provides a way of discerning whether variations in the inversion results are due to range-dependent features of the environment or simply uncertainty (variability) in the results.

The data considered here were taken from the MAPEX 2000 and BOUNDARY 2003 experiments, which were conducted in the Strait of Sicily, Mediterranean Sea. These experiments provided an excellent opportunity to investigate the inversion technique on different data sets recorded over essentially the same range-dependent track. There were several differences between the two experiments including the array lengths, sensor spacing and source frequencies. Ground-truth information in the form of core measurements and a high-resolution seismic profile were also available.

The ASSA algorithm was selected for the inversions after a careful evaluation of several inversion algorithms. This evaluation also included fast simulated annealing and genetic algorithms. The purpose of the study was to determine which algorithm induced the least amount of variability (i.e., found the optimal solution most reliably). The evaluation was carried out using synthetic noise-free and noisy data as well as MAPEX 2000 experimental data. It was found that ASSA generally obtained the lowest objective function value and introduced the least amount of variability.

Before inverting the measured data, ASSA was applied to realistic (noisy) synthetic data so that issues such as sediment layer resolution and parameter sensitivity could be assessed in a controlled manner. This type of analysis provides valuable insight into how to adapt the inversion for the experimental data. The study showed that the method was capable of estimating the range-dependent features of the environment by combining the individual range-independent inversion results. It also showed that the MAPEX 2000 data could resolve a three-layer environment when the layers were thick enough to influence the acoustic propagation; however, once the top layer became too thin (on the order of a meter), the data were no longer sensitive to it. For the BOUNDARY 2003 scenario it was found that the data could only resolve a two-layer environment and that the properties were not determined reliably. It should be noted that after the analysis of the experimental data it was shown that the SNR used for the synthetic study (10 dB) was slightly optimistic and that a SNR

of 5 dB would more closely approximate the experimental data.

ASSA was then applied to invert MAPEX 2000 and BOUNDARY 2003 experimental data. This analysis showed that the technique was able to estimate some of the range-dependent properties of the environment. The major issue was found to be choosing an appropriate environmental parameterization based on the resolving power of the data. This particular environment had the added complexity of a low-speed sediment inclusion for a portion of the track which, because it appears acoustically similar to the water column, makes it difficult to determine accurately the water depth and sediment properties of this layer. For the MAPEX 2000 scenario the data were only able to resolve a two-layer environment, but the resulting environment provided a good match to the ground-truth information. The BOUNDARY 2003 data were unable to resolve reliably the geoacoustic properties of the environment with the exception of the uppermost sediment properties.

The inversion analysis demonstrated that the MAPEX 2000 data produced results that were in better agreement with the ground-truth information (i.e., seismic and core data) and were more consistent from one inversion to another. This is likely due to two factors. First the array was considerably longer in the MAPEX 2000 case and therefore recorded acoustic energy that interacted with the bottom at a larger range of grazing angles. Second, the source used during BOUNDARY 2003 produced a swept signal that was at a higher frequency than during the MAPEX 2000 experiment which would result in a limited penetration depth into the sub-bottom.

The final aspect of the work in this thesis was the FGS analysis of the MAPEX 2000 experimental data. This is an important aspect because it provides a mechanism of ensuring that the variation in the ASSA inversion results (MAP estimates) is actually a result of the range-dependent environment and not simply the result of uncertainty/variability of the inversion results. The results of this analysis had two significant conclusions. First, there was good agreement between the FGS results

and the ground-truth information. Second, and most importantly, there was good agreement between these results and the MAP estimates. In particular, these results demonstrated that the large-scale variations were actually due to environmental range-dependence and not another source of variability. However, the smaller-scale variations appeared to be the result of uncertainty/variability in the MAP estimates.

This work has shown that combing the results from a series of short-range, range-independent inversions of HA data can provide the dominant range-dependent features of an environment. The techniques employed here were able to estimate the layering structure and sound speeds of the upper sediments (< 20 m), albeit with a somewhat simplified model of the environment. In general, this technique provides a viable method of estimating properties of range-dependent environments using HA data.

M. R. Fallat

References

Battle, D. J., Gerstoft, P., Kuperman, W. A., Hodgkiss, W. S., & Siderius, M. (2003). Geoacoustic inversion of tow-ship noise via near-field-matched-field processing. *IEEE Journal of Oceanic Engineering, 28*, 454–466.

Caiti, A., Jesus, S. M., & Kristensen, A. (1996). Geoacoustic seafloor exploration with a towed array in a shallow water area of the Strait of Sicily. *IEEE Journal of Oceanic Engineering, 21*, 355–366.

Chapman, N. R., Chin-Bing, S., King, D., & Evans, R. B. (2003). Benchmarking geoacoustic inversion methods for range dependent waveguides. *IEEE Journal of Oceanic Engineering, 28*, 320–331.

Chapman, N. R., Desert, J., Agarwal, A., Stephan, Y., & Demoulin, X. (2002). Estimation of seabed models by inversion of broadband acoustic data. *ACTA Acustica United with Acustica: The Journal of the European Acoustics Association, 88*, 756–759.

Chapman, N. R., Tolstoy, A., & Brooke, G. H. (1998). Workshop97: Benchmarking for geoacoustic inversion in shallow water. *Journal of Computational Acoustics, 6*, 1–28.

Collins, M. D. (1993). A split-step Padé solution for the parabolic equation method. *Journal of the Acoustical Society of America, 93*, 1738–1742.

Collins, M. D. (1994). Generalization for the split-step Padé solution. *Journal of the Acoustical Society of America, 96*, 382–385.

Collins, M. D., & Fishman, L. (1995). Efficient navigation of parameter landscapes. *Journal of the Acoustical Society of America, 98*, 1637–1644.

Collins, M. D., Kuperman, W. A., & Schmidt, H. (1992). Nonlinear inversion for ocean-bottom properties. *Journal of the Acoustical Society of America, 92*, 2770–2783.

Dosso, S. E. (2002). Quantifying uncertainty in geoacoustic inversion I. A fast Gibbs sampler approach. *Journal of the Acoustical Society of America, 111*, 129–142.

Dosso, S. E., & Nielsen, P. L. (2002). Quantifying uncertainty in geoacoustic inversion II. Application to broadband, shallow-water data. *Journal of the Acoustical Society of America, 111*, 143–159.

Dosso, S. E., Wilmut, M. J., & Lapinski, A.-L. S. (2001). An adaptive hybrid algorithm for geoacoustic inversion. *IEEE Journal of Oceanic Engineering, 21*, 324–336.

Dosso, S. E., Yeremy, M. L., Ozard, J. M., & Chapman, N. R. (1993). Estimation of ocean-bottom properties by matched-field inversion of acoustic field data. *IEEE Journal of Oceanic Engineering, 18*, 232–239.

Fallat, M. R. (1999). *Simplex simulated annealing, a hybrid approach to geoacoustic inversion with application to Mediterranean Sea acoustic data.* M.Sc. thesis, University of Victoria, Victoria, B.C., Canada.

Fallat, M. R., & Dosso, S. E. (1998). Geoacoustic inversion for the Workshop'97 benchmark test cases using simulated annealing. *Journal of Computational Acoustics, 6*, 29–43.

Fallat, M. R., & Dosso, S. E. (1999). Geoacoustic inversion via local, global and hybrid inversion. *Journal of the Acoustical Society of America, 105*, 3219–3230.

Fallat, M. R., Dosso, S. E., & Nielsen, P. L. (2004). An investigation of algorithm-induced variability in geoacoustic inversion. *IEEE Journal of Oceanic Engineering, 29*, 78–87.

Fallat, M. R., Nielsen, P. L., & Dosso, S. E. (2000). Hybrid geoacoustic inversion of broadband Mediterranean Sea data. *Journal of the Acoustical Society of America, 107*, 1967–1977.

Fallat, M. R., Nielsen, P. L., & Dosso, S. E. (2004). Estimating geoacoustic properties from towed horizontal array data. In D. G. Simons (Ed.), *Proceedings of the seventh european conference on underwater acoustics* (pp. 665–670). (ISBN: 90-5986-080-2)

Fallat, M. R., Nielsen, P. L., Dosso, S. E., & Siderius, M. (2005a). Characterization of a range-dependent environment from towed array data. In N. R. Chapman, A. Caiti, S. M. Jesus, & J.-P. Hermand (Eds.), *Proceedings of the second workshop on acoustic inversion methods and experiments for the assessment of the shallow water environment.* Kluwer Academic Publishers.

Fallat, M. R., Nielsen, P. L., Dosso, S. E., & Siderius, M. (2005b). Geoacoustic characterization of a range-dependent ocean environment using towed array data. *IEEE Journal of Oceanic Engineering, Accepted for Publication.*

Fallat, M. R., Nielsen, P. L., & Siderius, M. (2002). *The characterization of a range-dependent environment using towed horizontal array data from the MAPEX 2000 experiment* (Technical Memorandum, SM–402). La Spezia, Italy: NATO Undersea Research Centre.

Ferla, C. M., & Jensen, F. B. (2003). Are current environmental databases adequate for sonar predictions in shallow water? In N. G. Pace & F. B. Jensen (Eds.), *Proceedings of the impact of littoral environmental variability on acoustic predictions and sonar performance* (pp. 555–562). Kluwer Academic Publishers.

Gerstoft, P. (1994). Inversion of seismo-acoustic data using genetic algorithms and *a posteriori* probability distributions. *Journal of the Acoustical Society of America, 95*, 770–782.

Gerstoft, P. (1995). Inversion of acoustic data using a combination of genetic algorithms and the Gauss-Newton approach. *Journal of the Acoustical Society of America, 97*, 2181–2190.

Gerstoft, P. (1998). *SAGA Users manual 2.0, an inversion software package* (Technical Memorandum, SM–333). La Spezia, Italy: NATO Undersea Research Centre. (www.mpl.ucsd.edu/people/gerstoft)

Gerstoft, P., & Gingras, D. F. (1996). Parameter estimation using multifrequency range-dependent acoustic data in shallow water. *Journal of the Acoustical Society of America, 99*, 2839–2850.

Gerstoft, P., & Mecklenbräuker, C. F. (1998). Ocean acoustic inversion with estimation of *a posteriori* probability distributions. *Journal of the Acoustical Society of America, 104*, 808–819.

Gerstoft, P., & Michalopoulou, Z.-H. (1998). Global optimization in matched field inversion. In A. Alippi & G. B. Cannelli (Eds.), *Proceedings of the fourth european conference on underwater acoustics* (pp. 27–32).

Heard, G. J., Hannay, D., & Carr, S. (1998). Genetic algorithm inversion of the 1997 geoacoustic inversion workshop test case data. *Journal of Computational Acoustics, 6*, 61–71.

Jensen, F. B., Kuperman, W. A., Porter, M. B., & Schmidt, H. (1994). *Computational ocean acoustics*. New York, USA: AIP Press.

Jesus, S. M., & Caiti, A. (1996). Estimating geoacoustic bottom properties from a towed array data. *Journal of Computational Acoustics, 4*, 273–290.

Kirkpatrick, S., Gelatt, C. D., & Vecchi, M. P. (1983). Optimization by simulated annealing. *Science, 220*, 671–680.

Lindsay, C. E., & Chapman, N. R. (1993). Matched field inversion for geoacoustic model parameters using adaptive simulated annealing. *IEEE Journal of Oceanic Engineering, 18*, 224–231.

Liu, P., Hartzell, S., & Stephenson, W. (1995). Non-linear multiparameter inversion using hybrid global search algorithm: Applications in reflection seismology. *Geophysical Journal International, 122*, 991–1000.

Metropolis, N., Rosenbluth, A., M. Rosnebluth, A. T., & Teller, E. (1953). Equation of state calculations by fast computing machines. *Journal of Chemical Physics, 21*, 1087–1092.

Michalopoulou, Z.-H., & Ghosh-Dastidar, U. (2004). Tabu for matched-field source localization and geoacoustic inversion. *Journal of the Acoustical Society of America, 115*, 135–145.

Musil, M., Wilmut, M. J., & Chapman, N. R. (1999). A hybrid simplex genetic algorithm for estimating geoacoustic parameters using matched-field inversion. *IEEE Journal of Oceanic Engineering, 24*, 358–369.

Nelder, J. A., & Mead, R. (1965). A simplex method for function minimization. *Computer Journal, 7*, 308–311.

Osler, J., & Algan, O. (1999). *A high resolution seismic sequence analysis of the Malta Plateau* (Technical Report, SR–311). La Spezia, Italy: NATO Undersea Research Centre.

Park, C., Seong, W., Gerstoft, P., & Siderius, M. (2003). Time-domain geoacoustic inversion of high-frequency chirp signal from a simple towed system. *IEEE Journal of Oceanic Engineering, 28*, 468–478.

Pignot, P., & Chapman, N. R. (2001). Tomographic inversion of geoacoustic properties in a range-dependent shallow-water environment. *Journal of the Acoustical Society of America, 110*, 1338–1348.

Press, W. H., Teukolsky, S. A., Vetterling, W. T., & Flannery, B. P. (1992). *Numerical recipes in FORTRAN.* Cambridge, UK: Cambridge University Press.

Rajan, S. D., Lynch, J. F., & Frisk, G. V. (1987). Perturbative inversion methods for obtaining bottom geoacoustic parameters in shallow water. *Journal of the Acoustical Society of America, 82*, 998–1017.

Sen, M. K., & Stoffa, P. L. (1995). *Global optimization methods in geophysical inversions.* Amsterdam, NL: Elsevier Scientific Publishers.

Siderius, M., Gerstoft, P., & Nielsen, P. (1998). Broadband geoacoustic inversion from sparse data using genetic algorithms. *Journal of Computational Acoustics, 6*, 117–134.

Siderius, M., Nielsen, P. L., & Gerstoft, P. (2002). Range-dependent seabed characterization by inversion of acoustic data from a towed receiver array. *Journal of the Acoustical Society of America, 11*, 1523–1535.

Siderius, M., Nielsen, P. L., Sellschopp, J., Snellen, M., & Simons, D. (2001). Experimental study of geo-acoustic inversion uncertainty due to ocean sound-speed fluctuations. *Journal of the Acoustical Society of America, 110*, 769–781.

Snellen, M., Simons, D., Siderius, M., Sellschopp, J., & Nielsen, P. L. (2001). An evaluation of the accuracy of shallow water matched field inversion results. *Journal of the Acoustical Society of America, 109*, 514–527.

Snellen, M., Simons, D., & vanMoll, C. (2004). Application of differential evolution as an optimisation method for geo-acoustic inversion. In D. G. Simons (Ed.), *Proceedings of the 7th european conference on underwater acoustics* (pp. 721–726). (ISBN: 90-5986-080-2)

Szu, H., & Hartley, R. (1987). Fast simulated annealing. *Physics Letters A, 122*, 157–162.

Tarantola, A. (1987). *Inverse problem theory: Methods for data fitting and model parameter estimation.* Amsterdam, NL: Elsevier Scientific Publishers.

Tolstoy, A. (1998). MFP benchmark inversions via the RIGS method. *Journal of Computational Acoustics, 6*, 185–203.

vanMoll, C., & Simons, D. (2004). Improved performance of global optimisation methods for inversion problems in underwater acoustics. In D. G. Simons (Ed.), *Proceedings of the 7th european conference on underwater acoustics* (pp. 715–720). (ISBN: 90-5986-080-2)

Westwood, E. K., & Tindle, C. T. (1987). Shallow water time series simulation using ray theory. *Journal of the Acoustical Society of America, 81*, 1752–1761.

Westwood, E. K., Tindle, C. T., & Chapman, N. R. (1996). A normal mode model for acousto-elastic ocean environments. *Journal of the Acoustical Society of America, 100*, 3631–3645.

Westwood, E. K., & Vidmar, P. J. (1987). Eigenray finding and time series simulation in a layered-bottom ocean. *Journal of the Acoustical Society of America, 81*, 912–924.

Zala, C., & Ozard, J. M. (1998). Estimation of geoacoustic parameters from narrowband data using a search-optimization technique. *Journal of Computational Acoustics, 6*, 223–243.